

Toward Perfect Optical Diffusers: Dielectric Huygens' Metasurfaces with Critical Positional Disorder

Dennis Arslan,* Aso Rahimzadegan,* Stefan Fasold, Matthias Falkner, Wenjia Zhou, Maria Kroychuk, Carsten Rockstuhl, Thomas Pertsch, and Isabelle Staude*

Conventional optical diffusers, such as thick volume scatterers (Rayleigh scattering) or microstructured surface scatterers (geometric scattering), lack the potential for on-chip integration and are thus incompatible with next-generation photonic devices. Dielectric Huygens' metasurfaces, on the other hand, consist of 2D arrangements of resonant dielectric nanoparticles and therefore constitute a promising material platform for ultrathin and highly efficient photonic devices. When the nanoparticles are arranged in a random but statistically specific fashion, diffusers with exceptional properties are expected to come within reach. This work explores how dielectric Huygens' metasurfaces can implement wavelength-selective diffusers with negligible absorption losses and nearly Lambertian scattering profiles that are largely independent of the angle and polarization of incident waves. The combination of tailored positional disorder with a carefully balanced electric and magnetic response of the nanoparticles is shown to be an integral requirement for the operation as a diffuser. The proposed metasurfaces' directional scattering performance is characterized both experimentally and numerically, and their usability in wavefront-shaping applications is highlighted. Since the metasurfaces operate on the principles of Mie scattering and are embedded in a glassy environment, they may easily be incorporated in integrated photonic devices, fiber optics, or mechanically robust augmented reality displays.

1. Introduction

Optical diffusers are key elements in various applications as diverse as illumination,^[1–3] imaging,^[4–7] screens,^[8] microscopy,^[9–13] colorants,^[14–16] spectroscopy,^[17–19] photovoltaics,^[20–22] or wavefront shaping.^[23–25] Their main use is to spread light across a large solid angle, thereby minimizing or ideally removing glares or high-intensity bright spots.^[26,27]

A variety of optical diffusers based on different concepts have been developed and are commonly employed, among which are volume diffusers^[28–30] like opal glass, microstructured surface diffusers^[31–35] like ground glass, and holographic diffusers.^[36–39] Volume diffusers based on Rayleigh scattering of deep-subwavelength scatterers provide an almost Lambertian light distribution, but at the cost of low energy efficiency. Microstructured surface diffusers offer relatively high transmission efficiencies, but only limited control over the spatial distribution of scattered light.

D. Arslan, I. Staude
Institute of Solid State Physics
Friedrich Schiller University Jena
07743 Jena, Germany
E-mail: dennis.arslan@uni-jena.de; isabelle.staude@uni-jena.de

D. Arslan, S. Fasold, M. Falkner, W. Zhou, T. Pertsch, I. Staude
Institute of Applied Physics
Abbe Center of Photonics
Friedrich Schiller University Jena
07745 Jena, Germany


A. Rahimzadegan, C. Rockstuhl
Institute of Theoretical Solid State Physics
Karlsruhe Institute of Technology
76131 Karlsruhe, Germany
E-mail: aso.rahimzadegan@kit.edu

A. Rahimzadegan, C. Rockstuhl
Karlsruhe School of Optics and Photonics
Karlsruhe Institute of Technology
76131 Karlsruhe, Germany

M. Kroychuk
Faculty of Physics
Lomonosov Moscow State University
Moscow 119991, Russia

C. Rockstuhl
Institute of Nanotechnology
Karlsruhe Institute of Technology
76021 Karlsruhe, Germany

C. Rockstuhl, T. Pertsch, I. Staude
Max Planck School of Photonics
Albert-Einstein-Str. 7, 07745 Jena, Germany

 The ORCID identification number(s) for the author(s) of this article can be found under <https://doi.org/10.1002/adma.202105868>.

© 2021 The Authors. Advanced Materials published by Wiley-VCH GmbH. This is an open access article under the terms of the Creative Commons Attribution-NonCommercial License, which permits use, distribution and reproduction in any medium, provided the original work is properly cited and is not used for commercial purposes.

DOI: 10.1002/adma.202105868

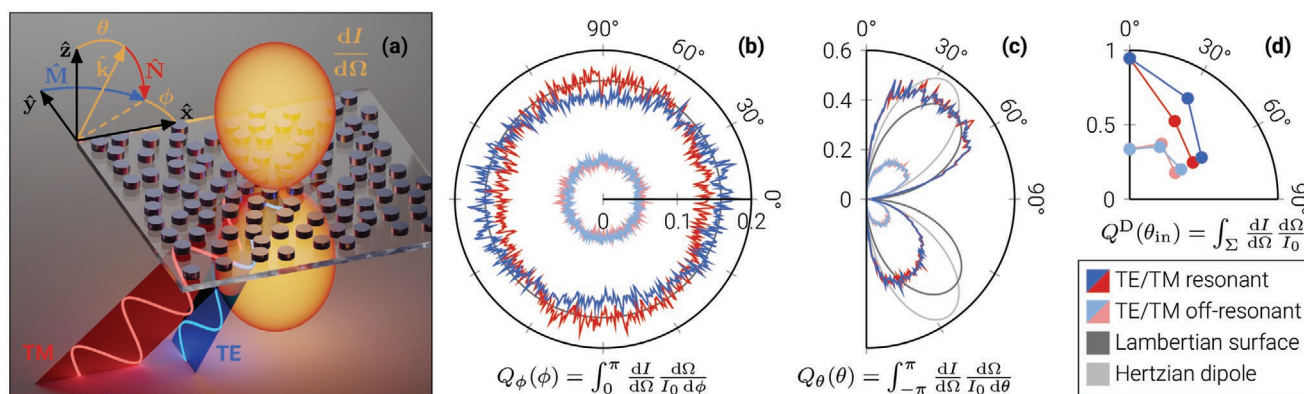


Figure 1. What is a perfect optical diffuser? a) Artistic impression of a positionally disordered metasurface with a scattering profile (orange; scattered intensity I per unit solid angle $d\Omega = \sin\theta d\phi d\theta$) that hardly changes when excited by generic TE-polarized (blue) or TM-polarized (red) plane waves. b,c) The azimuthal (b) and polar (c) scatterance show the fraction of the incident intensity I_0 per unit angle that is scattered along all polar or azimuthal angles, respectively, when the metasurface is excited by a normally incident plane wave near (saturated colors) or off (desaturated colors) its resonance wavelength. Scatterances of ideal scatterers are shown for comparison. d) The diffuse scatterance, as a function of the incidence angle θ_{in} of a plane wave, is the efficiency with which a metasurfaces redistributes the incident energy across all diffuse directions Σ . For reference: (b–d) show simulations of the soft-core uniform metasurface type for the overlapping resonance case with resonant ($\lambda = 1.38 \mu\text{m}$) and off-resonant ($\lambda = 1.52 \mu\text{m}$) excitation.

Holographic diffusers are carefully engineered surface diffusers that offer high transmission efficiencies and tailored spatial light distributions. However, their optical response is usually very sensitive to the incidence angle and polarization, and since most surface diffusers require a defined index contrast at their surface, they cannot readily be deployed in changing environments.

Rapid developments in nanotechnology and an ever-growing push for miniaturization drive the reimplementations of conventional optical elements with ever smaller footprints. The need for efficient and ultrathin optical diffusers becomes particularly more pressing with the continuous replacement of conventional light bulbs by flat light sources. Conventional optical diffusers are bulky^[8,24,40–43] and lack the capability to be integrated into flat photonic devices.^[44–46] Metasurfaces, consisting of designed optical nanoparticles arranged in a planar fashion, can overcome this limitation and enable optical devices with a subwavelength thickness.^[47–55]

Disordered metasurfaces constitute an auspicious material platform for the diffusion of light.^[56–58] Concentrating initially on ordered arrangements of plasmonic nanoresonators, various disordered metasurfaces were described in the literature and shown to support wavelength-selective diffuser functionalities while exhibiting additional unique features such as a tailorable scattering profile,^[59–61] or a large optical memory effect due to their flatness and isotropic disorder.^[62] Furthermore, their use as polarization-independent^[63] and high-information-capacity^[64] wavefront shaping elements and artificial chiral media^[65] was explored.

More recently, the focus in metasurface research shifted toward all-dielectric implementations,^[44,66–72] which offer the additional advantages of low losses, enhanced in-plane coupling, and a multipolar response. As such, dielectric disordered metasurfaces were demonstrated to allow for high-numerical-aperture wavefront-shaping with a large memory effect^[56] and structural color generation^[16,73] with an improved insensitivity concerning the viewing angle.

Moreover, dielectric Huygens' metasurfaces^[74–78] show a particularly rich optical response.^[79–84] In such metasurfaces, the electric and magnetic moments that are excited in the scattering

elements by a normally incident plane wave have equal scattering strength. This electromagnetic duality symmetry condition^[85–87] results in a suppressed zeroth-order reflectance in periodic structures. Previously, we demonstrated the emergence of a disorder-induced phase transition in positionally disordered dielectric Huygens' metasurfaces.^[88] We observed that the zeroth-order transmittance reduces to zero for a critical degree of positional disorder. Since a perfect optical diffuser requires the suppression of both the zeroth-order reflectance and transmittance, the disorder-induced phase transition takes a central role in the present work.

Another advantage of resonant metasurfaces is their ability to simultaneously implement different optical functionalities at different wavelengths.^[89] While most commercially available diffusers are broadband, efforts to render their performance wavelength-selective are, with a few exceptions,^[90,91] so far limited to the use of colored glass as diffuser material. However, colored glass only introduces absorption and does not alter the scattering characteristics of the diffuser. Thus, a diffuser that diffuses at one or a discrete set of wavelengths only, while letting all other wavelengths pass undisturbed, would offer intriguing new opportunities in applications such as fluorescence microscopy, augmented reality displays,^[92] or holographic displays^[93] with interactive features.

In this work, we demonstrate that disordered dielectric Huygens' metasurfaces allow for the realization of wavelength-selective and nearly perfect optical diffusers. We consider a perfect diffuser to exhibit zero absorption losses and a Lambertian scattering profile, both in transmission and reflection, that is independent of the incidence angle and polarization. The realized metasurface diffusers have only a subwavelength thickness, which is crucial for a large memory effect, and feature a robust planar surface, which favors their use not only in solid matrices, but also in various liquids and gasses. Furthermore, already very small pixel sizes of a few square micrometers are sufficient to achieve the desired diffuser performance, which is of particular interest in application areas such as integrated optics, fiber optics, or displays.

Figure 1 illustrates the properties of a perfect optical diffuser and motivates the physical quantities which we will use for its characterization. The artistic impression in **Figure 1a** depicts a positionally disordered metasurface with a scattering profile, intensity per solid angle $dI/d\Omega$, that hardly changes for different plane wave excitations. Since we do not aim for a particular application scenario, we will compare our metasurfaces with ideal scatterers that show equal hemispherical transmittance and reflectance. In particular, we consider a Lambertian surface and a Hertzian dipole for reference. For an easier comparison of shapes, we normalize the scattering profile by the incident intensity I_0 and integrate over all azimuthal (**Figure 1b**) or polar (**Figure 1c**) angles. Note that since the differential solid angle $d\Omega \propto \sin(\theta)$ vanishes along the polar axis, **Figure 1c** inherits the $\sin(\theta)$ factor and **Figure 1b** effectively excludes contributions from regular directions (here: zeroth-order transmission and reflection). **Figure 1b** and **Figure 1c** show the simulated optical response of a fabricated metasurface with a disordered arrangement as depicted in **Figure 1a** when the metasurface is excited directly at or slightly off its resonance wavelength by a normally incident plane wave. Clearly, the optical response is almost independent of the incident polarization, and for off-resonant excitation, the metasurface scatters considerably less light along diffuse directions, that is, nonregular directions. The scattering profile is highly uniform along the azimuthal direction, slightly asymmetric along the polar direction, and has a shape similar to the reference scatterers. Last, **Figure 1d** shows the integral of the normalized scattering profile across all diffuse directions. This quantity measures how efficiently a metasurface diffuses the incident energy. As the incidence angle increases, less light is scattered along diffuse directions. However, while holographic diffusers typically only accept incidence angle deviations of a few degrees, the presented metasurface allows a few tens of degrees.

In the following discussion, we first elaborate on the design and fabrication of four dielectric Huygens' metasurfaces with different degrees of positional disorder. Then, we experimentally and numerically study their spectral features in the zeroth-order transmission and reflection for oblique and normal incidence. This spectral analysis provides insight into the fundamental working mechanisms of our metasurfaces. We also statistically evaluate the spatial distribution of transmittance and phase values, as well as induced dipole moments across the metasurface plane. Here we observe opportunities for wavefront shaping with disordered metasurfaces and show that positional disorder effectively maintains the electromagnetic duality symmetry. Finally, we conclude with a detailed numerical and experimental study of the directional transmission and reflection of all disordered metasurfaces for different incidence angles and excitation wavelengths.

2. Results and Discussion

2.1. Metasurface Types and Resonance Cases

We devised four metasurface types with various degrees of positional disorder, which we labeled as array, perturbed array, soft-core uniform and hard-core uniform. Each metasurface type represents a unique 2D arrangement of identical nanocylinders

made of amorphous silicon and embedded in amorphous silicon dioxide. The array metasurface type is a square lattice with a lattice constant of a , which we consider a perfectly ordered reference structure for the remaining disordered metasurface types. The perturbed array is based on a square lattice, where a random vector translates each lattice point with a magnitude $<a/2$. The uniform-type metasurfaces are obtained from a generalized Matérn point process^[88,94,95] which generates isotropic and homogeneous point distributions. While the hard-core uniform type only enforces a minimum clearance radius around each nanocylinder, the soft-core uniform type also enforces a linearly increasing probability of finding any other nanocylinder in an annulus spanning from the clearance radius to a radius of one lattice constant.

Furthermore, we designed two resonance cases for which the effective electric dipole resonance (ED) and magnetic dipole resonance (MD) of the nanocylinders of a metasurface type are either spectrally overlapping at a wavelength of about 1.4 μm or separate at about 1.5 μm (MD) and 1.6 μm (ED). We fixed the nanocylinder diameter and height in each resonance case and targeted the same average density $\rho = 1/a^2$ for all metasurface types.

A full description of all metasurface types and resonance cases can be found in the Experimental Section ("Metasurface Types and Resonance Cases"), which also provides technical details on the design strategies and the geometric parameters of the fabricated metasurfaces. In the fabrication, we applied a process based on electron-beam lithography and reactive-ion etching, which is further specified in the Experimental Section ("Fabrication"). Technical details about all experiments and simulations are listed in the Experimental Section ("Experiments" and "Simulations", respectively).

Figure 2 shows pair correlation functions and scanning electron microscopy images of the disordered metasurface types. The 2D pair correlation function $g(\mathbf{r})$ compares the local particle density at the point \mathbf{r} of a particle system with that of an ideal gas, where \mathbf{r} is measured with respect to an arbitrary reference particle of the system. The radial pair correlation function $g(r)$ is the azimuthal average of $g(\mathbf{r})$. The corresponding structure factors are shown in **Figure S1**, Supporting Information, and their numerical computation and relationship with the pair correlation function are outlined in the Experimental Section ("Pair Correlation Function and Structure Factor").

While the perturbed array maintains the long-range order of the underlying array^[96] (**Figure 2b**), the uniform-types exhibit a long-range order that is comparable to an ideal gas (**Figure 2c** and **Figure 2d**), and a short-range order that is almost entirely limited to a length scale of a few lattice constants (**Figure 2a** for $r/a < 2$). At this point, it can already be expected that the optical response of the array-type metasurfaces will be dominated by their crystal-like structure, and that the isotropy of the uniform-type metasurfaces will translate to an insensitivity concerning the polarization and orientation of an incident plane wave.

2.2. Zeroth-Order Transmission and Reflection

This section discusses the influence of positional disorder on the spectral and spatial features in the zeroth-order transmission and reflection of all metasurfaces.

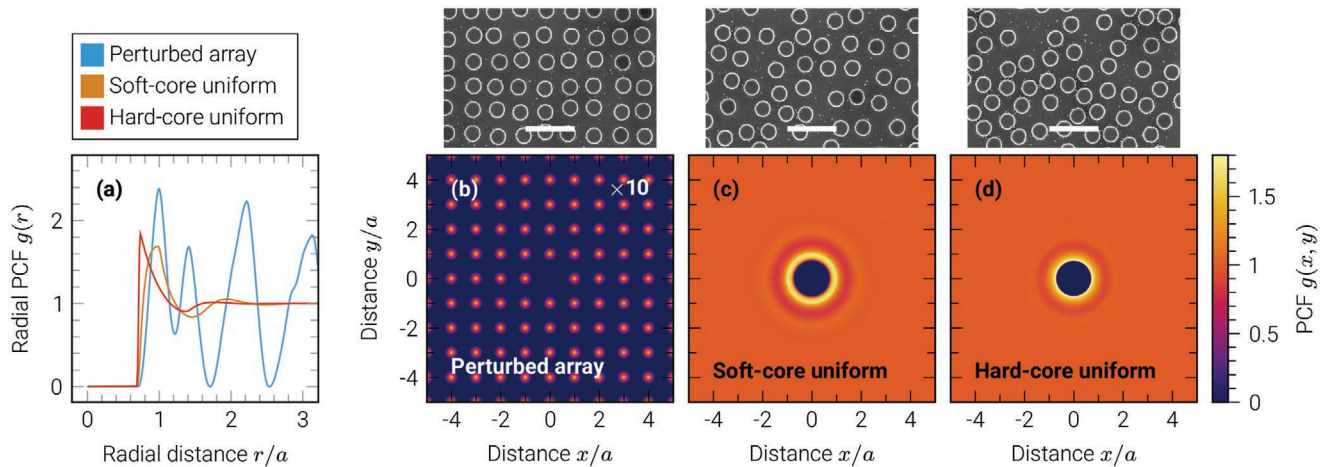


Figure 2. Pair correlation functions (PCFs) of disordered metasurface types. a) Radial and b–d) 2D pair correlation functions of the perturbed array (b), soft-core uniform (c), and hard-core uniform (d) metasurface types for the overlapping resonance case. Corresponding scanning electron microscopy images of fabricated metasurfaces are placed above (b–d) with scale bars of 1.6 μm . The values in (b) are ten times larger than indicated by the color bar. All distances are normalized with respect to the lattice constant $a = 800$ nm of the array.

We begin with the particularization of the physical setting (Figure 1a): We assume a Cartesian coordinate system $\mathbf{r} = x\hat{\mathbf{x}} + y\hat{\mathbf{y}} + z\hat{\mathbf{z}}$, where $\hat{\mathbf{z}}$ is normal to the metasurface and points into the direction of transmission. The metasurface is embedded in a homogeneous, isotropic medium with refractive index n . The plane wave wavevector \mathbf{k} is expressed in terms of its polar $\theta \in [0, \pi]$ and azimuthal $\phi \in [-\pi, \pi]$ propagation angle

$$\mathbf{k}(\theta, \phi) = k_0 \hat{\mathbf{k}}(\theta, \phi) \quad (1)$$

$$\hat{\mathbf{k}}(\theta, \phi) = \sin(\theta)\cos(\phi)\hat{\mathbf{x}} + \sin(\theta)\sin(\phi)\hat{\mathbf{y}} + \cos(\theta)\hat{\mathbf{z}} \quad (2)$$

where $k_0 = 2\pi n/\lambda$ is the wavenumber and λ the vacuum wavelength. It can be shown that the electric field vectors of TE ($\mathbf{M}_{\mathbf{k}}$) and TM ($\mathbf{N}_{\mathbf{k}}$) polarized plane waves

$$\mathbf{M}_{\mathbf{k}}(\mathbf{r}) = ie^{i\mathbf{k}\cdot\mathbf{r}}\hat{\mathbf{M}}_{\mathbf{k}} \quad \hat{\mathbf{M}}_{\mathbf{k}} = \hat{\mathbf{k}} \times \hat{\mathbf{z}}/\sin(\theta) \quad (3)$$

$$\mathbf{N}_{\mathbf{k}}(\mathbf{r}) = -e^{i\mathbf{k}\cdot\mathbf{r}}\hat{\mathbf{N}}_{\mathbf{k}} \quad \hat{\mathbf{N}}_{\mathbf{k}} = \hat{\mathbf{k}} \times \hat{\mathbf{M}}_{\mathbf{k}} \quad (4)$$

form a complete basis in homogeneous, isotropic media.^[97]

With this, we may write the electric field of a TE or TM polarized incident plane wave in terms of

$$\mathbf{E}_{\text{in}}^{\text{X}}(\mathbf{r}) = E_{\text{in}}^{\text{X}} \begin{cases} \mathbf{M}_{\mathbf{k}_{\text{in}}}(\mathbf{r}) & \text{X: TE} \\ \mathbf{N}_{\mathbf{k}_{\text{in}}}(\mathbf{r}) & \text{X: TM} \end{cases} \quad (5)$$

where E_{in}^{X} is its amplitude and \mathbf{k}_{in} its wavevector. Considering the possibility of polarization conversion from X to Y, we may define the generalized transmission coefficient as

$$t_{\mathbf{k}}^{\text{X,Y}} = \frac{1}{E_{\text{in}}^{\text{X}}} \begin{cases} \langle \mathbf{M}_{\mathbf{k}}^*(\mathbf{r}) \cdot \mathbf{E}(\mathbf{r}) \rangle & \text{Y: TE} \\ \langle \mathbf{N}_{\mathbf{k}}^*(\mathbf{r}) \cdot \mathbf{E}(\mathbf{r}) \rangle & \text{Y: TM} \end{cases} \quad (6)$$

where \mathbf{E} is the electric field transmitted by the metasurface, $\langle \cdot \rangle$ is an area-averaging integral across the metasurface plane, and \mathbf{k} is the direction of the transmitted plane wave. For brevity, we refer to the zeroth-order co-polarized transmission coefficient simply as transmission coefficient t , and define the transmittance T and phase φ as:

$$t = t_{\mathbf{k}_{\text{in}}}^{\text{X,X}} \quad T = |t|^2 \quad \varphi = \arg(t) \quad (7)$$

The zeroth-order reflection coefficient r and the reflectance $R = |r|^2$ are defined analogously to Equations (6) and (7), in which \mathbf{k}_{in} must be replaced by its reflection.

Furthermore, by omitting the integrals in Equation (6), we obtain from Equation (7) the transmission coefficient profile $t(\mathbf{r})$, the transmittance profile $T(\mathbf{r})$ and the phase profile $\varphi(\mathbf{r})$. We quantify the spatial distribution of transmittance and phase values with means μ_T, μ_φ and variances $\sigma_T^2, \sigma_\varphi^2$, where the ring accents emphasize the circular nature of the phase angle and the usage of corresponding circular moments. See Experimental Section (“Probability Density Functions”) for a detailed description of these statistical quantities.

Last, we define the diffuse scatterance as

$$Q^D = \int_{\Sigma} \frac{dI}{d\Omega} \frac{d\Omega}{I_0} = \int_{\Sigma} Q_{\Omega} |\cos(\theta)| d\Omega \quad (8)$$

where $\Sigma = \{(\theta, \phi) \mid \hat{\mathbf{k}}(\theta, \phi) \neq \hat{\mathbf{k}}_i\}$ represents all possible directions excluding countably many $\hat{\mathbf{k}}_i$, and Q_{Ω} is the directional scatterance as defined by Equation (12). We call Σ the set of diffuse directions and $\hat{\mathbf{k}}_i$ the regular directions. Moreover, we chose the rather uncommon term scatterance as hypernym for transmittance and reflectance as to emphasize on the radiometric terminology and the unification of the half-spaces. Consequently, we use the diffuse scatterance to measure how efficiently a metasurface redistributes light from regular directions across all diffuse directions. For a fair comparison between different metasurface types, we consider all diffraction orders of the array as the regular directions of the array-type metasurfaces,

and the directions along which a flat surface refracts or reflects an incident plane wave (i.e., the zeroth orders of the array) as the regular directions of the uniform-type metasurfaces. In the absence of gain and absorption loss, for negligible cross-polarization, and if only the zeroth orders can be excited, the diffuse scatterance simplifies to $Q^D = 1 - T - R$. See Sections S1 and S2, Supporting Information, for a detailed derivation of the quantities involved in Equation (8).

2.2.1. Spectral Features for Oblique Incidence

Figure 3 shows experimental transmittance spectra of all metasurface types and resonance cases for TE or TM polarized plane wave excitation with incidence angles $\theta_{in} \leq 20^\circ$ and $\phi_{in} = 0^\circ$. Here, all angles are measured with respect to air, and the lattice vectors of the array-type metasurfaces are aligned with \hat{x}, \hat{y} . In the following discussion, we always refer to the transmittance values at resonance wavelengths.

The array behaves as expected:^[80] In the overlapping resonance case and for normal incidence (Figure 3a, $\theta_{in} = 0^\circ$), the

ED and MD are in spectral overlap. Due to this equal electric-magnetic response, negligible absorption, and discrete rotational symmetry of the arrangement, the reflectance is suppressed, and consequently, the transmittance is near one. As the incidence angle increases, the ED and MD shift apart and separate at about 15° (TE) or 10° (TM), while the transmittance reduces to near zero. In the separate resonance case (Figure 3b) and for TM polarization, the ED and MD shift toward each other and overlap at about 13.5° , which leads to a high transmittance due to the generalized Brewster effect.^[98] The comparatively narrow resonances at wavelengths of about 1.25 and $1.30 \mu\text{m}$ in Figure 3a, and 1.40 and $1.45 \mu\text{m}$ in Figure 3b, are higher-order lattice modes that are not excited under normal incidence. These experimental transmittance spectra are in excellent agreement with simulations (Figure S2, Supporting Information).

The resonance wavelengths of the perturbed array are almost identical to those of the array. However, the presence of positional disorder significantly reduces the transmittance when the ED and MD are in spectral overlap (compare Figure 3a and Figure 3c for $\theta_{in} < 10^\circ$ and Figure 3b and Figure 3d for

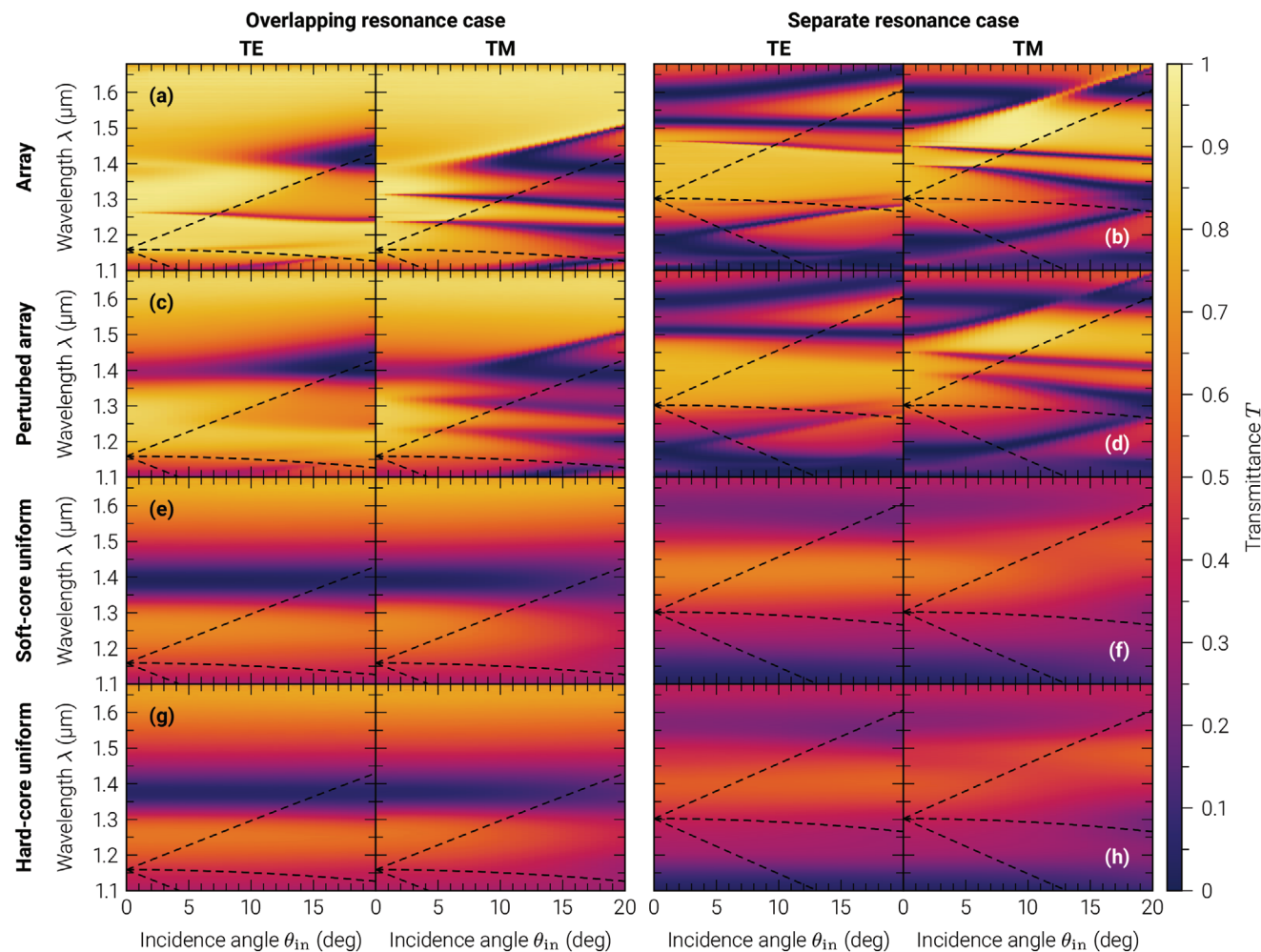


Figure 3. Experimental transmittance spectra for oblique incidence. a–h) Transmittance spectra of the array (a,b), perturbed array (c,d), soft-core uniform (e,f), and hard-core uniform (g,h) metasurface type for the overlapping (a,c,e,g) and separate (b,d,f,h) resonance case with TE- or TM-polarized plane wave excitation. The dashed lines indicate the onset of the lowest diffraction orders in the array (top to bottom: (1, 0), (0, ± 1), (-1, 0)).

$\theta_{in} = 13.5^\circ$), and slightly broadens and increases the transmittance when the ED and MD are spectrally separate.

The uniform-types show only minuscule differences compared to each other, but a much stronger insensitivity regarding the incidence angle and polarization when compared to the array-types. In the overlapping resonance case (Figure 3e and Figure 3g), the transmittance is near zero, and the ED and MD hardly shift as the incidence angle increases. In the separate resonance case (Figure 3f and Figure 3h), the transmittance is considerably higher, and the ED and MD are spectrally much broader than in the perturbed array. Extended simulations confirm the observed trends for incidence angles of up to 45° (Figure S3, Supporting Information)

In summary, the uniform-type metasurfaces of the overlapping resonance case exhibit properties which make them promising candidates for perfect diffusers. On the one hand, they show a near-zero transmittance, which is a necessary, though insufficient, requirement for a high diffuse scatterance. On the other hand, they are highly insensitive to the incidence angle and polarization, which is interesting for applications that require a large numerical aperture. The following subsection and “Theory of Disordered Huygens’ Metasurfaces” in the

Experimental Section provide deeper insight in the physical mechanisms that lead to the observed effects.

2.2.2. Spectral Features for Normal Incidence

In this subsection, we sort all metasurface types according to their degree of positional disorder, identify those which are close to a disorder-induced phase transition,^[88] and provide a more detailed description of how positional disorder influences their zeroth-order transmission and reflection spectra. In the following discussion, we focus on TE polarized plane wave excitation under normal incidence.

First, consider the transmittance and phase spectra of the overlapping resonance case for increasing wavelengths (Figure 4a and Figure 4c). For the array-type metasurfaces, the transmittance remains relatively high while the phase shows normal dispersion and a cumulative phase change of about -2π . For the uniform-type metasurfaces, the transmittance reaches near zero when the phase exhibits anomalous dispersion, and the cumulative phase change is almost zero. Alternatively, we may imagine the corresponding transmission coefficient

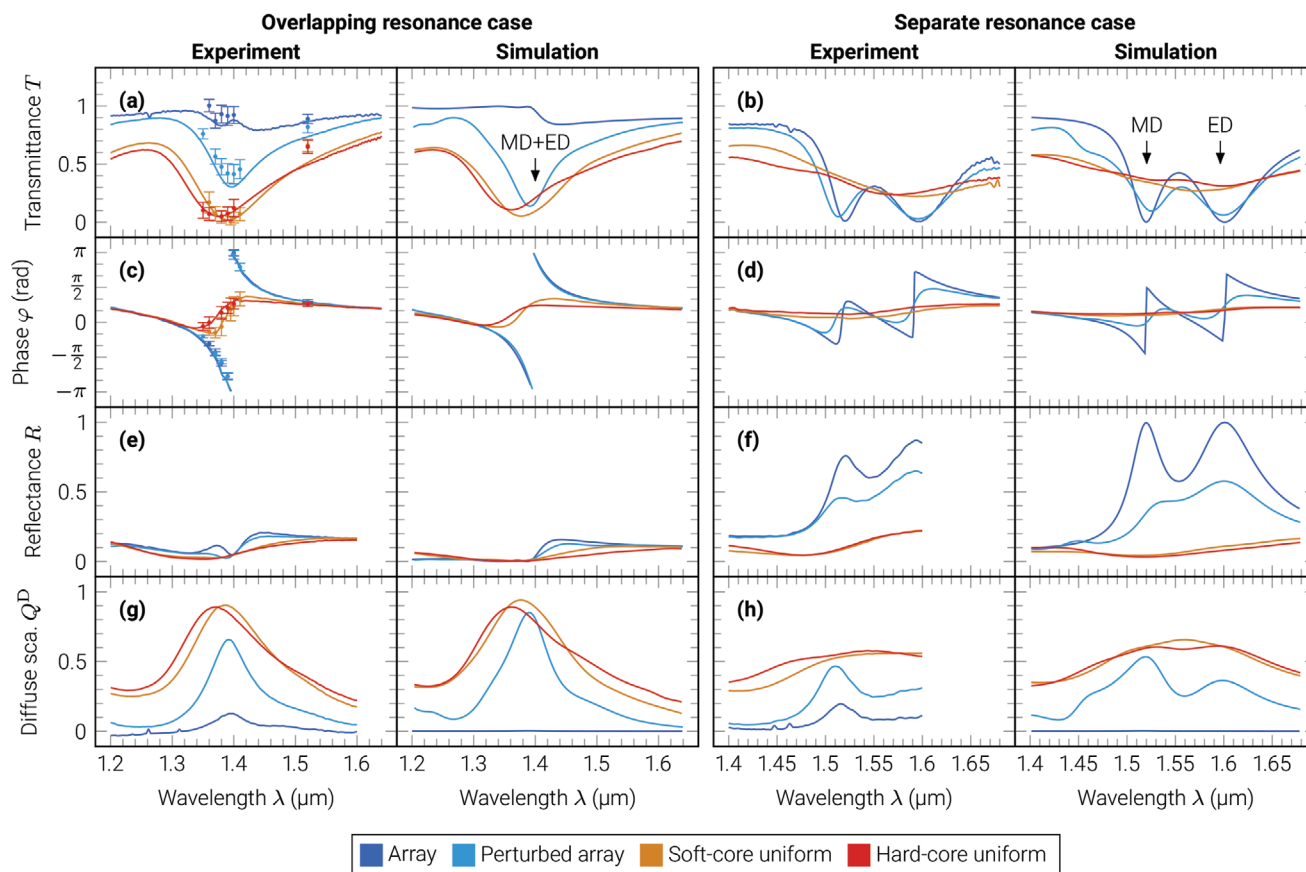


Figure 4. Spectra for normal incidence. a–h) Experimental and simulated transmittance (a,b), phase (c,d), reflectance (e,f), and diffuse scatterance (g,h) spectra for the overlapping (a,c,e,g) and separate (b,d,f,h) resonance cases with TE-polarized plane wave excitation under normal incidence. Experimental spectra were measured in an incoherent white-light spectroscopy setup and a Fourier transform interferometer. The error bars show the spatial mean and standard deviation of experimental transmittance and phase profiles, which were measured in an imaging phase-shifting interferometer. The labels MD and ED indicate the resonance wavelength of the magnetic and electric dipole resonance, respectively. Here, we evaluated the special case $Q^D = 1 - T - R$.

spectra $t(\lambda) = \sqrt{T(\lambda)} \exp(i\varphi(\lambda))$ as parametric curves in the complex plane (cf., Figure S4a, Supporting Information). For the array-type metasurfaces, $t(\lambda)$ circles once around the origin of the complex plane, whereas for the uniform-type metasurfaces, the curve remains in one quadrant of the complex plane and only approaches the origin near the resonance wavelength. The same behavior was observed in metasurfaces similar to the perturbed array type,^[88] where a gradual increase in positional disorder results in a continuous transformation of $t(\lambda)$ from a curve that circles the origin to a curve that resides in one quadrant. This implies the existence of a critical degree of positional disorder, at which $t(\lambda)$ passes exactly through the origin and an abrupt disorder-induced phase transition from normal to anomalous dispersion occurs. In other words, increasing positional disorder first decreases the transmittance at the resonance wavelength to zero, but then increases it again once the phase transitioned to anomalous dispersion. With this, we sort the metasurface types in the sequence of increasing positional disorder: array, perturbed array, soft-core uniform, hard-core uniform. Furthermore, soft-core uniform shows the smallest transmittance at resonance and is therefore closest to the disorder-induced phase transition.

In the separate resonance case (Figure 4b and Figure 4d), increasing positional disorder always increases the transmittance at the resonance wavelengths, while the phase spectra flatten and the phase remains in the anomalous dispersion regime. Similar to the discussion of the overlapping resonance case, this behavior is best understood in the complex plane (cf., Figure S4b, Supporting Information): The array metasurface type possesses a curve $t(\lambda)$ that does not circle the origin, which corresponds to a state that already exceeds the critical degree of positional disorder. Consequently, any increase in positional disorder drives the system only further away from the phase transition, and the effects mentioned above can be observed.

Moreover, the reflectance and diffuse scatterance spectra of the separate resonance case show that at the resonance wavelengths (Figure 4f and Figure 4h), increasing positional disorder reduces the reflectance and increases the diffuse scatterance. However, even for the maximal positional disorder (hard-core uniform), the lowest reflectance still amounts to about 5% and the highest diffuse scatterance only to about 60%. This is in stark contrast to the reflectance and diffuse scatterance in the overlapping resonance case (Figure 4e and Figure 4g): The reflectance at the resonance wavelength is zero for all metasurface types, and the diffuse scatterance approaches one near the critical degree of positional disorder (soft-core uniform). As the wavelength is tuned away from the resonance, the diffuse scatterance reduces significantly. For example, nearly 80% of the incident light passes undisturbed through the soft-core uniform metasurface at $\lambda = 1.6 \mu\text{m}$. This demonstrates the wavelength-selective diffuser functionality of the disordered metasurfaces, which could be further engineered, for example, by including carefully tailored higher-order multipoles.^[81]

With this, we conclude that the soft-core uniform metasurface type of the overlapping resonance case is most suitable for the operation as a perfect diffuser. The remaining question of how the metasurfaces redistribute the incident energy along the diffuse directions will be addressed in Section 2.3.

2.2.3. Spatial Features for Normal Incidence

In the remainder of this section, we focus on the overlapping resonance case and study spatial statistics for resonant ($\lambda = 1.38 \mu\text{m}$) and off-resonant ($\lambda = 1.52 \mu\text{m}$) excitation by a TE polarized plane wave under normal incidence. More precisely, we statistically evaluate the spatial transmittance and phase profiles as well as the effective dipole moments that are induced in the nanocylinders of each metasurface type (see “Effective Dipole Moments” in the Experimental Section). With this study, we aim to characterize the influence of positional disorder in Huygens’ metasurfaces, and provide a basis for the discussion of how such metasurfaces may be employed in wavefront shaping applications.

First, we obtained transmittance and phase profiles, constructed kernel density estimates of their 2D probability density functions (PDFs), and computed marginal PDFs by integrating over one variable of the 2D PDFs.^[99] The profiles are displayed in Figure S5, Supporting Information, for reference. Figure 5a and Figure 5b show experimental and simulated PDFs $f(\varphi, T)$, where metasurface types are color-coded, and excitation wavelengths and mean values are indicated by marks. The differences between experiment and simulation in terms of the mean values are mainly due to a slight mismatch in the resonance wavelengths, which can also be seen in Figure 4a and Figure 4c near the excitation wavelengths. In the simulations, we computed $t(\mathbf{r})$ with a spatial resolution of about $\lambda/3$ and accounted for the limited numerical aperture ($\text{NA} = 0.25$) and the camera pixel size ($5 \mu\text{m}$, square) of the experimental setup with the application of corresponding low-pass filters. We want to emphasize that the phase distributions are indeed uniform on a microscopic level (Figure S6d–g, Supporting Information), and that the following distributions mainly result from the local spatial averaging of the transmitted electric field. The marginal PDFs of the phase $f(\varphi)$ (Figure 5c and Figure 5d) closely resemble wrapped normal distributions, and the variances in the simulated phase agree well with the experiment. The marginal PDFs of the transmittance $f(T)$ (Figure 5e and Figure 5f) slightly deviate from a folded normal distribution, and the variances in the simulated transmittance are systematically smaller than in the experiment. However, this is most likely due to external influences in the experiment, as for example imperfections in the sample and the excitation beam. With these limitations in mind, we consider our simulations to predict the spatial transmittance and phase distributions of all metasurface types realistically, which will be the basis for a detailed study of directional transmission and reflection in Section 2.3.

To reveal the influence of positional disorder on the mean and standard deviation of the transmittance and phase profiles, we assembled scatter plots (Figure 6a and Figure 6b) from the experimental data in Figure 5 and from a few additional measurements near the resonance wavelength as indicated by the error bars in Figure 4a and Figure 4c. The sole purpose of these additional measurements is to visualize the wavelength-sensitivity of the statistical quantities near the resonance.

Figure 6a relates the standard deviation of the transmittance (σ_T) with that of the phase (σ_φ). For off-resonant excitation,

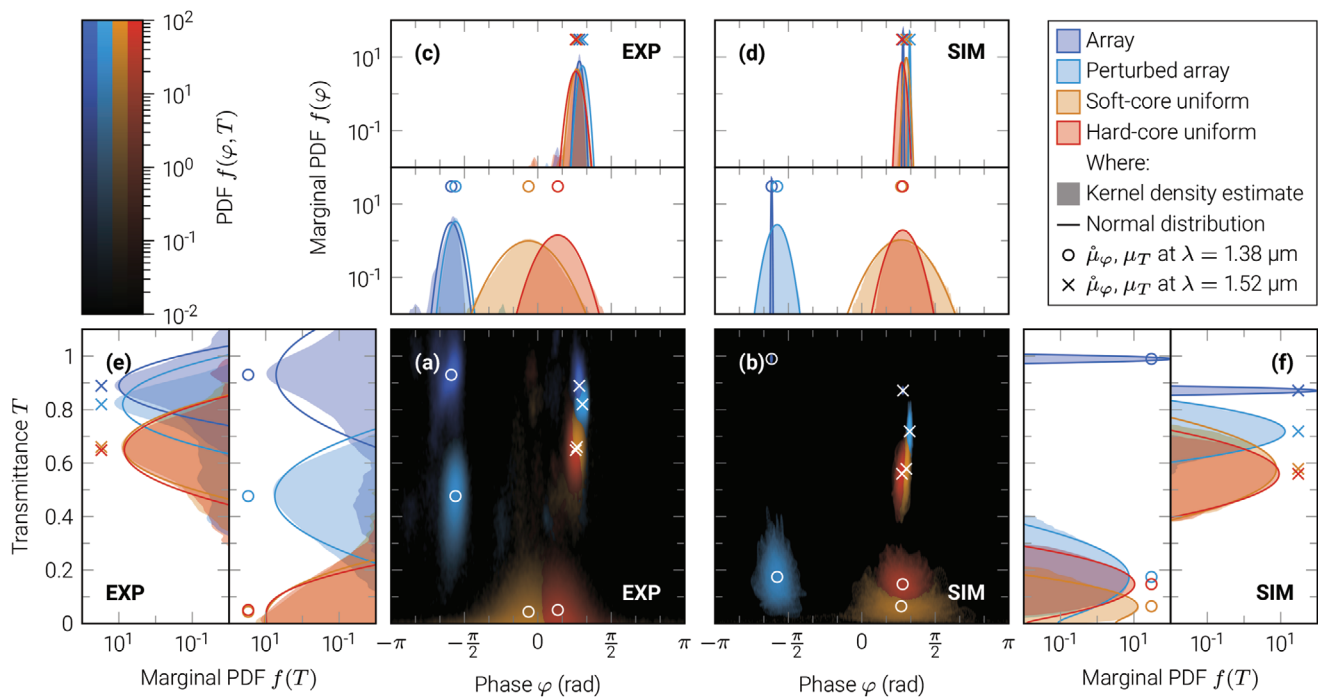


Figure 5. Probability density functions (PDFs) of transmittance and phase profiles. a, b) The maximum $\max_{\tau\lambda} f_{\tau\lambda}(\varphi, T)$ of the PDFs $f_{\tau\lambda}$ of all metasurface types τ (encoded by different colors) for the overlapping resonance case with resonant ($\lambda = 1.38 \mu\text{m}$) and off-resonant ($\lambda = 1.52 \mu\text{m}$) excitation (encoded by different marks) by a TE-polarized plane wave under normal incidence. c–f) Marginal PDFs, that is, integrals of $f_{\tau\lambda}(\varphi, T)$ along φ or T , where shaded areas result from kernel density estimates and solid lines show wrapped (c,d) and folded (e,f) normal distributions with matching means and variances. a, c, e) Experimental (EXP) and b, d, f) simulated (SIM) data.

both σ_T and $\hat{\sigma}_\varphi$ increase with increasing positional disorder. As the excitation wavelength is tuned to the resonance, the array-type metasurfaces exhibit a positive correlation between σ_T and $\hat{\sigma}_\varphi$. In contrast, the uniform-type metasurfaces show that $\hat{\sigma}_\varphi$ increases almost independently of σ_T . For resonant excitation, we observe that $\hat{\sigma}_\varphi$ is higher the closer a metasurface is to the disorder-induced phase transition.

However, it should be noted that the primary cause for this increase in $\hat{\sigma}_\varphi$ may not be a positional disorder, but rather a

vanishing mean transmittance (μ_T). Figure 6b shows that $\hat{\sigma}_\varphi$ and μ_T are strongly correlated and follow a relationship that is almost independent of positional disorder: As μ_T decreases to zero, the distribution of $\varphi(\mathbf{r})$ becomes more uniform and $\hat{\sigma}_\varphi$ follows with an exponential increase.

Furthermore, note that perturbed arrays with varying degrees of positional disorder constitute an exciting platform for wavefront shaping applications that require both amplitude and phase modulation in transmission. The high similarity

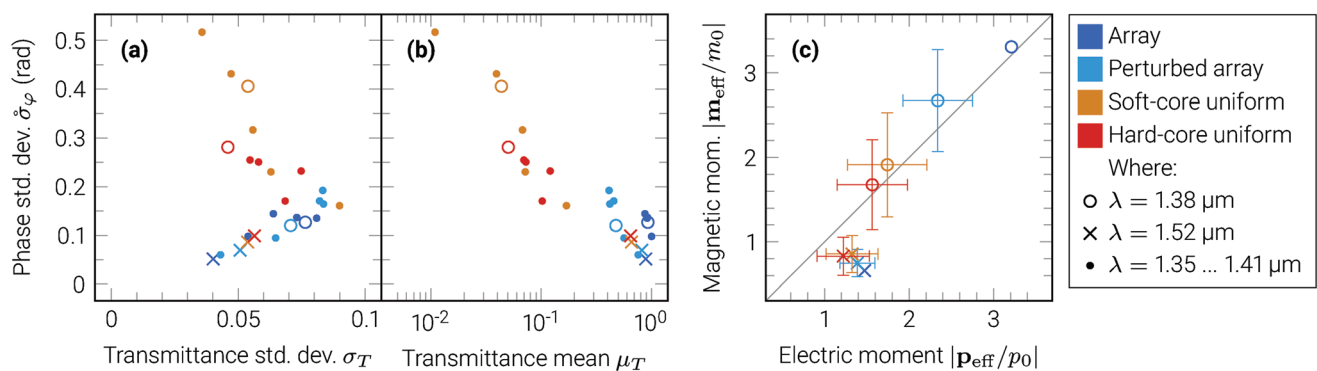


Figure 6. The influence of positional disorder on spatial statistics. a, b) Scatter plots for the overlapping resonance case with TE polarized plane wave excitation under normal incidence, showing the standard deviation of experimental phase profiles with respect to the standard deviation (a) and mean (b) of the corresponding transmittance profiles, and c) the mean (marks) and standard deviation (error bars) of simulated effective dipole moments that are induced in the nanocylinders of a metasurface. The circles and crosses indicate resonant ($\lambda = 1.38 \mu\text{m}$) and off-resonant ($\lambda = 1.52 \mu\text{m}$) excitation. The dots show additional measurements near the resonance. The data in (a, b) correspond to the error bars in Figure 4a and Figure 4c. The gray line in (c) indicates the equal electric and magnetic moment condition.

in the $\sigma_T\text{-}\hat{\sigma}_\phi$ -dependencies (Figure 6a) of the perturbed array and the array suggests that they perform equally well in zeroth order. As will be shown later, the perturbed array does indeed scatter more light along diffuse directions than the array, but this can be taken into account in simulations, and some applications may even benefit from it, as for example transmission holograms where a higher numerical aperture or a more uniform intensity distribution could be achieved. Additionally, the phase spectrum (Figure 4c) of the perturbed array is almost identical to that of the array, whereas the transmittance at the resonance wavelength (Figure 4a) is a function of the degree of positional disorder. Hence, we may see positional disorder as an additional degree of freedom in the design of wavefront shaping applications.

Finally, to obtain a clearer picture of how positional disorder affects the response of individual nanocylinders, we simulated the induced effective electric and magnetic dipole moments in 100 central nanocylinders of each metasurface type and evaluated their mean and standard deviation (Figure 6c). For off-resonant excitation, the induced moments are small in magnitude, they deviate from the equal electric–magnetic moment condition (gray line), and positional disorder slightly increases their standard deviation. On the other hand, the standard deviations are much larger for resonant excitation, but also significantly more nanocylinders are at or close to the equality condition. As a result, the combination of resonant excitation and positional disorder can greatly spread the induced dipole moments, but the collective response of all nanocylinders remains close to the electric–magnetic equality condition.

2.3. Directional Transmission and Reflection

This section first presents the simulated directional transmission and reflection of the disordered metasurface types and studies their response to different excitations, before we evaluate the experimental directional transmission of all metasurface types for similar excitations. We do not aim for a strict comparison of simulated and experimental results since the simulations assume a homogeneous background, whereas the experiments involve reflections at air/substrate interfaces and other technical complications. Instead, we introduce the simulations in the sense of an ideal model that provides a theoretical understanding of the involved physical processes and assesses the performance of the fabricated metasurfaces with respect to the ideal situation. We consider resonant and off-resonant TE polarized plane wave excitation for normal and oblique incidence. Corresponding data for TM polarized excitation can be found in the Supporting Information.

In the following, we define several quantities which are closely related to standard radiometric quantities, and are based on the transmitted $\mathbf{E}^T(\mathbf{r})$ and reflected $\mathbf{E}^R(\mathbf{r})$ electric field on the respective side of a metasurface. We want to emphasize that this involves the total electric field and not the scattered field formalism as known from Mie theory. From plane wave expansions of the electric fields (Section S1, Supporting Information) and a careful evaluation of the area-average $\langle \cdot \rangle$ of the time-averaged Poynting vector $\mathbf{S}(\mathbf{r})$ across the metasurface

plane, we obtain an integral expression for the area-averaged intensity $I = |\langle \mathbf{S} \rangle \cdot \hat{\mathbf{z}}|$, where the integrand can be interpreted as a directional intensity

$$\frac{d^2 I(\mathbf{k})}{dk_x dk_y} = \frac{d^2}{dk_x dk_y} \begin{cases} I^T(\mathbf{k}) & k_z \geq 0 \\ I^R(\mathbf{k}) & k_z < 0 \end{cases} \quad (9)$$

that unifies the transmitted I^T and reflected I^R directional intensities resulting from \mathbf{E}^T and \mathbf{E}^R , respectively. Furthermore, we are able to relate the directional intensity with the area-averaged radiance L

$$L(\theta, \phi) = \frac{dI(\theta, \phi)}{|\cos(\theta)| d\Omega} = k_0^2 \left. \frac{d^2 I(\mathbf{k})}{dk_x dk_y} \right|_{\mathbf{k}=\mathbf{k}(\theta, \phi)} \quad (10)$$

where $d\Omega = \sin(\theta)d\phi d\theta$ is the unit solid angle.

Motivated by this relationship, we define the directional scatterance $Q_\Omega = L/I_0$, the directional transmittance Q_Ω^T , and the directional reflectance Q_Ω^R

$$Q_\Omega(\mathbf{k}) = \frac{k_0^2}{I_0} \frac{d^2 I(\mathbf{k})}{dk_x dk_y} = \begin{cases} Q_\Omega^T & k_z \geq 0 \\ Q_\Omega^R & k_z < 0 \end{cases} \quad (11)$$

$$Q_\Omega(\theta, \phi) = \frac{1}{I_0} \frac{dI(\theta, \phi)}{|\cos(\theta)| d\Omega} = Q_\Omega(\mathbf{k}(\theta, \phi)) \quad (12)$$

where I_0 is the intensity of an arbitrarily polarized incident plane wave, and the subscript Ω indicates units of inverse steradians. While $Q_\Omega(\theta, \phi)$ is the fraction of the incident intensity scattered along (θ, ϕ) into a projected unit solid angle, $Q_\Omega(\mathbf{k})$ can be understood as the normalized intensity recorded in the back-focal-plane of a lens that collects the light scattered off the metasurface.

A full integral over Q_Ω yields the scatterance $Q = Q^T + Q^R$, which is simply the sum of the hemispherical transmittance Q^T and the hemispherical reflectance Q^R . Note that in the absence of gain and absorption loss, $Q = 1$ due to energy conservation. While the scatterance may not be very useful on its own, its differential representations allow computation of how efficiently a metasurface scatters into a given solid angle.

With this, we further define the azimuthal scatterance Q_ϕ and the polar scatterance Q_θ

$$Q_\phi(\phi) = \frac{dQ(\phi)}{d\phi} = \int_0^\pi Q_\Omega(\theta, \phi) \sin(\theta) |\cos(\theta)| d\theta \quad (13)$$

$$Q_\theta(\theta) = \frac{dQ(\theta)}{d\theta} = \int_{-\pi}^\pi Q_\Omega(\theta, \phi) \sin(\theta) |\cos(\theta)| d\phi \quad (14)$$

which have units of inverse radians and can be interpreted as marginal integrals of Q_Ω , or as the azimuthal and polar contributions to Q . Since Q_Ω typically contains strong speckles, we found Q_ϕ and Q_θ to be the most reliable measures for the comparison of the shape of Q_Ω with that of an ideal scatterer. Other similarity measures, as for example normalized cross-correlations, tend to produce results which are dominated by the speckle pattern.

In order to provide absolute values on how much energy flows into a given solid angle, we define the cumulative integral of Q_θ as the sectorial scatterance $Q(\theta)$

$$Q(\theta) = \int_0^\theta Q_\theta(\theta') d\theta' + \Delta(\theta) \quad (15)$$

where the piece-wise constant function $\Delta(\theta)$ (Equation (S39), Supporting Information) is an integration constant that accounts for jump discontinuities in the critical points $\theta \in \{0, \pi\}$ such that $Q(\pi) = Q$. In other words, $Q(\theta)$ is the fraction of the incident intensity scattered into a spherical sector with a half-angle of θ . Consequently, we find that $Q^T = Q(\pi/2)$ and $Q^R = Q(\pi) - Q(\pi/2)$.

As ideal scatterers, we consider a Lambertian surface with a directional scatterance of $Q_\Omega^L(\theta, \phi) = 1/(2\pi)$ and a Hertzian dipole with $Q_\Omega^H(\theta, \phi) = 3/(4\pi) |\cos(\theta)|$.

Last, since the contributions of TE and TM polarized scattered waves are additive, they can easily be separated as in $Q = Q^{TE} + Q^{TM}$, where Q may stand for any of the previously defined scatterance variables.

2.3.1. Simulated Scatterance

Figure 7 shows the simulated scatterance of the disordered metasurface types for TE polarized plane wave excitation with incidence angles of $\theta_{in} = \{0^\circ, 30^\circ, 60^\circ\}$ and $\phi_{in} = 0^\circ$. Here, all propagation angles are measured with respect to the background medium (SiO_2). Furthermore, since the directional scatterance $Q_\Omega(\mathbf{k})$ in Figure 7a and Figure 7b is mirror-symmetric with respect to the k_x - k_z -plane, we display transmission only for $k_y > 0$ and reflection only for $k_y < 0$. Figure S7, Supporting Information, shows the corresponding situation for TM polarized excitation.

For resonant excitation and normal incidence, the directional scatterance Q_Ω (Figure 7a, $\theta_{in} = 0^\circ$) of the uniform-type metasurfaces is highly uniform along the azimuthal angle, while that of the perturbed array shows a weak azimuthal dependency. As the incidence angle increases, the uniform-type metasurfaces transmit slightly more light along directions perpendicular to the incident wave, while the perturbed array scatters increasingly more light along regular directions. The same trends can be observed for off-resonant excitation (Figure 7b), with the exception that already at normal incidence, most light is scattered along regular directions. Note that the regular directions can also be seen as peaks in the polar scatterance Q_θ (Figure 7c and Figure 7d), or as jumps in the sectorial scatterance $Q(\theta)$ (Figure 7e and Figure 7f). For example, the height of the step $Q(\theta_{in})$ represents the fraction of the incident energy that is contained in the zeroth order in transmission.

In summary, we observe a redistribution of energy from diffuse directions toward regular directions as the incidence angle increases, or as the excitation wavelength is tuned away from the resonance. This demonstrates that the presented metasurfaces heavily rely on the excitation of matched dipole moments to achieve a high diffuse scatterance. However, since these metasurfaces were designed to have equal electric and magnetic dipole moments for normal incidence, it may be possible

to achieve a high diffuse scatterance with an optimized nanocylinder arrangement for other incidence angles as well.

For resonant excitation and increasing incidence angle, the polar scatterance (Figure 7c) of the uniform-type metasurfaces remains almost unchanged and comparable to a Hertzian dipole for up to about $\theta_{in} \leq 30^\circ$. The perturbed array performs similarly well at normal incidence since it adequately suppresses the zeroth orders (cf., Figure 7e). At larger incidence angles, however, the polar scatterance of the perturbed array significantly reduces along diffuse directions as the higher diffraction orders of the underlying array become available as new radiation channels. These diffraction orders can be seen as additional peaks in the polar scatterance, and are not present in the uniform-type metasurfaces. Interestingly, for large transmission angles $\theta \in [45^\circ, 90^\circ]$, the polar scatterance of all disordered metasurface types even exceeds that of a Hertzian dipole and is comparable to a Lambertian surface (cf., Figure 1c). However, this surplus in transmission also implies less energy in reflection.

For resonant excitation and increasing incidence angle, the sectorial scatterance (Figure 7e) further reveals that the fraction of cross-polarized light $Q^{TM}(180^\circ)$ decreases faster in the perturbed array than in the uniform-type metasurfaces.

2.3.2. Experimental Scatterance

Figure 8 shows the experimental scatterance of all metasurface types for TE polarized plane wave excitation with incidence angles of $\theta_{in} = \{0^\circ, 10^\circ, 20^\circ\}$ and $\phi_{in} = 0^\circ$. Here, all measurements were performed in transmission, and all propagation angles are measured with respect to air. We intentionally did not normalize the experimental data with respect to the background medium of the simulations, since the total internal reflection at the substrate-air interfaces in the experiments, as discussed in the following paragraphs, cannot be resolved unambiguously and would therefore lead to misleading comparisons. Figure S8, Supporting Information, shows the corresponding situation for TM-polarized excitation.

The directional scatterance in Figure 8a and Figure 8b was measured in a back-focal-plane-imaging setup with the procedure described in the Experimental Section ("Experiments"). The array metasurface type demonstrates the limitations of the experimental setup. Ideally, the array should exhibit only one Dirac-delta-like peak, but the transfer function of the collecting microscope objective and secondary reflections from the substrate led to a broadening of the zeroth-order peak and the emergence of a secondary peak. However, it should be noted that the transfer function is nearly diffraction-limited and that one might easily overestimate its full width at half maximum ($k_{FWHM}/k_0 \approx 0.005$ at $\lambda = 1.38 \mu\text{m}$) due to the clipped logarithmic color scale.

Furthermore, in the following discussion, it should be kept in mind that scattered waves with polar angles of about $\theta \geq 44^\circ$ experience total internal reflection at the substrate-air interfaces. These secondary waves may again be scattered by the metasurface or exit on the sides of the substrate. However, this appears to be rather a technological complication than a fundamental limitation, which could be lifted by designing the directional scatterance of the embedded metasurface

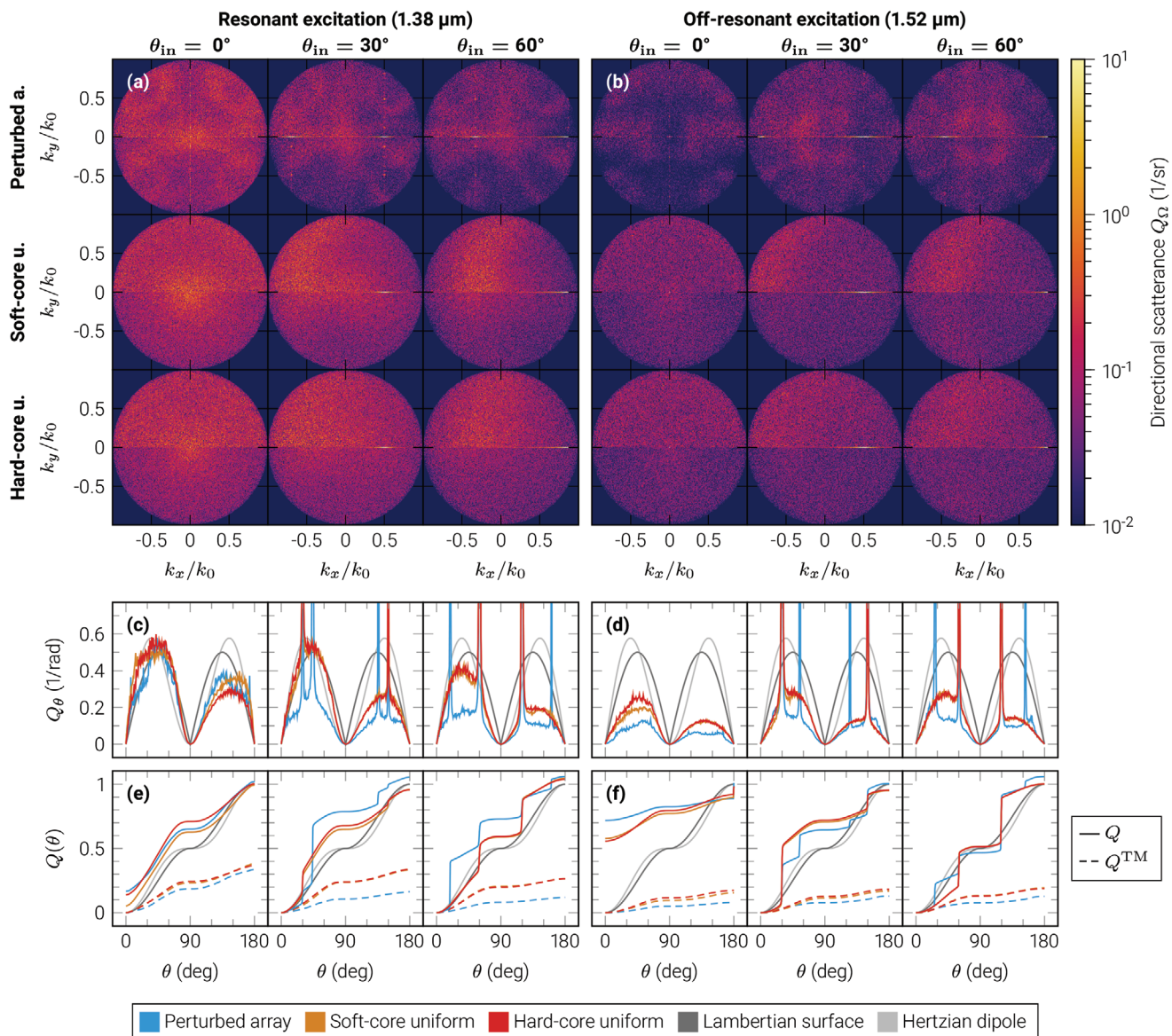


Figure 7. Simulated scattering for TE-polarized excitation. a–f) The directional Q_{Ω} (a,b), polar Q_{θ} (c,d), and sectorial $Q(\theta)$ (e,f) scattering of the perturbed array, soft-core uniform, and hard-core uniform metasurface type for the overlapping resonance case with resonant ($\lambda = 1.38 \mu\text{m}$) (a,c,e) or off-resonant ($\lambda = 1.52 \mu\text{m}$) (b,d,f) excitation by a TE-polarized plane wave incident under $\theta_{\text{in}} \in \{0^\circ, 30^\circ, 60^\circ\}$. The column and row titles indicate all parameter combinations. In (a,b), $k_y > 0$ shows transmission and $k_y < 0$ reflection. In (e,f), Q^{TM} shows the contribution of cross-polarized light to $Q = Q^{\text{TE}} + Q^{\text{TM}}$. All wavenumbers are normalized with respect to the magnitude of the wavevector k_0 in SiO_2 .

such that it vanishes in the region of total internal reflection, or more trivially, by operating the diffuser in an index-matched environment. The ability to tailor the reciprocal space with positional disorder has already been demonstrated in hyperuniform plasmonic metasurfaces.^[60] While there was recent progress in the efficient generation of point distributions with a prescribed pair correlation functions or structure factor,^[100,101] it remains the question of how to efficiently and accurately compute the directional scattering from the structure factor of a dense and highly resonant metasurface, that is, beyond the Born approximation. In this context, the following experimental results may be seen as a first step toward realizing a perfect optical diffuser.

Overall, the directional scattering in the experiment (Figure 8a and Figure 8b) shows the same dependency on the incidence angle and the excitation wavelength as in the simulation (Figure 7a and Figure 7b). It is also higher and more isotropic in the uniform-type metasurfaces than in the perturbed array.

For resonant excitation and large polar angles, the experimental polar scattering (Figure 8c) of the uniform-type metasurfaces appears similar to a Hertzian dipole, which can be seen as a constant offset with respect to the Hertzian dipole curve. However, the sectorial scattering (Figure 8e) suggests that the uniform-type metasurfaces hardly exceed 25% hemispherical transmittance. The perturbed array shows a much higher

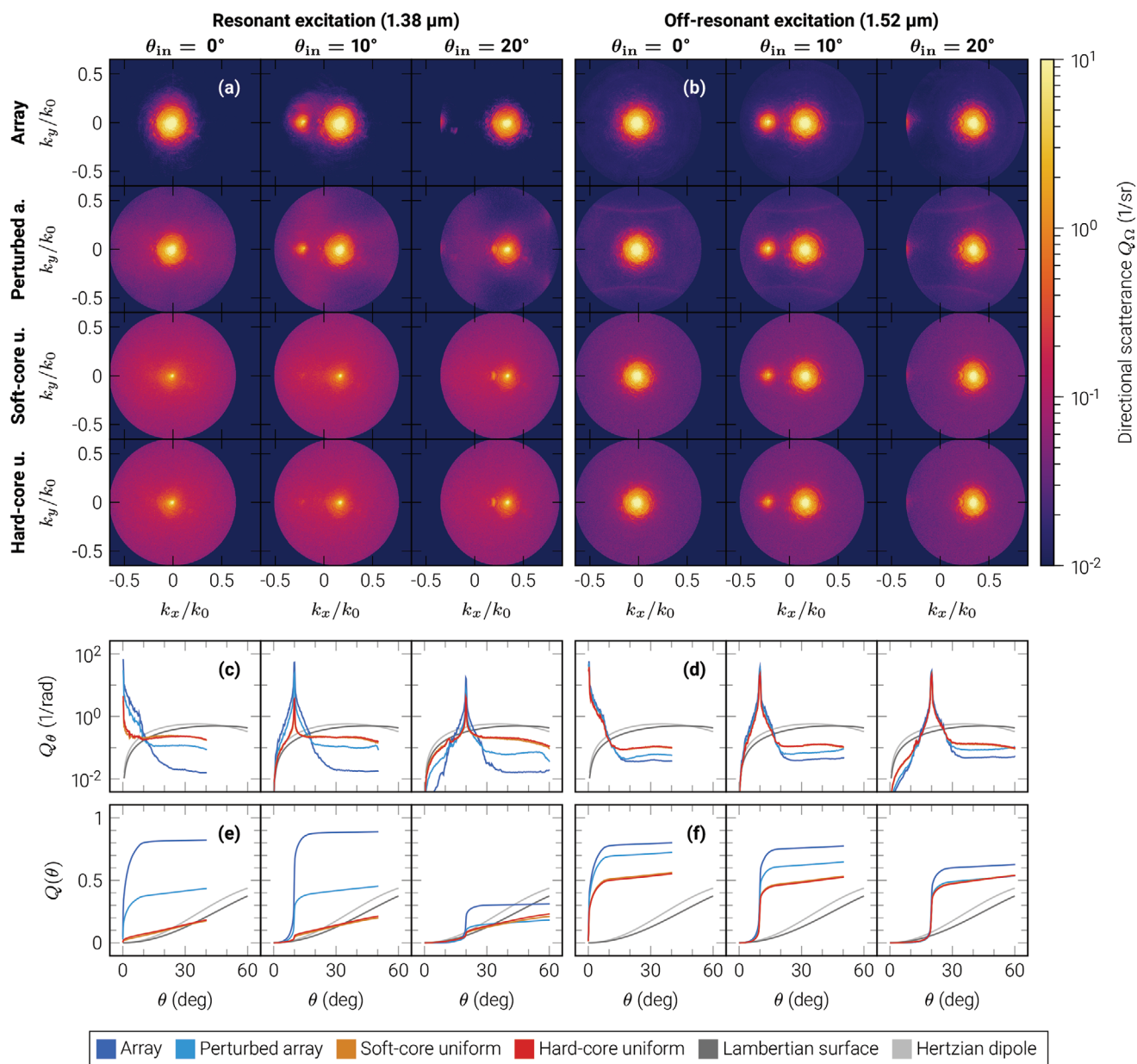


Figure 8. Experimental scatterance for TE polarized excitation. a–f) The directional Q_{Ω} (a,b), polar Q_{θ} (c,d), and sectorial $Q(\theta)$ (e,f) scatterance of the array, perturbed array, soft-core uniform, and hard-core uniform metasurface type for the overlapping resonance case with resonant ($\lambda = 1.38 \mu\text{m}$) (a,c,e) or off-resonant ($\lambda = 1.52 \mu\text{m}$) (b,d,f) excitation by a TE polarized plane wave incident under $\theta_{\text{in}} \in \{0^\circ, 10^\circ, 20^\circ\}$. All graphs show transmission ($k_z \geq 0$, $\theta \leq 90^\circ$). The column and row titles indicate all parameter combinations. All wavenumbers are normalized with respect to the magnitude of the wavevector k_0 in air.

hemispherical transmittance, mostly due to a high zeroth-order transmittance. The lower hemispherical transmittance in the experiment may be explained by secondary waves that are mainly scattered back into the hemisphere associated with reflection, or which are guided to the sides of the substrate.

Nevertheless, the experimental results show that the fabricated uniform-type metasurfaces strongly suppress the zeroth-order transmittance, scatter similarly to a Hertzian dipole, tolerate a wide range of incidence angles, and are wavelength-selective.

3. Conclusion

We have presented the particle statistics of three types of disordered metasurfaces, where the particle positions were taken from a perturbed square array or a generalized Matérn point process. We chose these methods since they guarantee a minimum distance between any pair of particles and allow the generation of a few million particle positions with relatively little computational effort. Although generalizations of the collective-coordinate method^[100] can generate particle positions

with a prescribed structure factor, which may be the most direct approach to reciprocal space engineering, it is yet unclear how to accurately predict the optical response of our resonant metasurfaces from the structure factor. Due to this circumstance, we followed a heuristic approach where we targeted the same average particle density in all metasurfaces and investigated two uniform particle distributions with similar but distinct short-range order.

We experimentally studied the zeroth-order transmittance of all proposed metasurfaces for oblique incidence. The uniform-type metasurfaces showed spectral features which are virtually independent of the incidence angle and polarization.

Experimental and simulated spectra at normal incidence provided a deeper physical understanding of the interplay between positional disorder and the excited electric and magnetic dipole resonances. Near the disorder-induced phase transition, we observe that the diffuse scatterance approaches one, indicating that no light is scattered along the zeroth order in transmission and reflection. However, for off-resonant excitation, most of the light is transmitted along the zeroth order. This is a first indication that metasurfaces with critical disorder may be employed as wavelength-selective diffusers.

We also studied the spatial distribution of transmittance and phase values and induced effective dipole moments. Here, we saw that perturbed arrays might be suitable for wavefront shaping, and that uniform positional disorder effectively preserves the equality of the electric–magnetic induced moments.

Finally, we characterized the directional transmission and reflection of our metasurfaces. On the one hand, we performed accurate simulations to cover the full reciprocal space for the situation where the metasurface is embedded in a homogeneous background medium. Here we observe scattering profiles similar to Lambertian surfaces or Hertzian dipoles. As the incidence angle increases, the scattering profiles mostly maintain their shape along diffuse directions, but increasingly more energy resides in the regular directions.

On the other hand, we performed experimental measurements, which include an additional glass–air interface that leads to total internal reflection. We did not account for this in our design, as it would require reciprocal space engineering. However, to overcome the influence of total internal reflection, it would suffice to limit the scattered light to a cone with a half-angle equal to the critical angle. As this relaxes the necessity to scatter along large angles, one may also employ nanoparticles with a more directional far-field emission. Nevertheless, considering this difference with respect to the simulations, we observe the same effects as theoretically predicted, but with a slightly reduced hemispherical transmittance of about 25%.

In summary, we have presented the theoretical basis and experimental proof of concept for the design and fabrication of disordered metasurfaces that may be employed as wavelength-selective perfect diffusers.

4. Experimental Section

Metasurface Types and Resonance Cases: Table 1 summarizes the targeted and actual geometric parameters of all metasurface types for both resonance cases. Due to fabrication requirements, a minimum

Table 1. Targeted and actual (in square brackets) geometric parameters for the overlapping and separate resonance case.

| Nanocylinder | Resonance case | | | | | |
|--------------------|----------------|--------------------|-------------|--------|----------|--------|
| | | | Overlapping | | Separate | |
| Diameter | d | nm | 490 | [468] | 600 | [582] |
| Height | h | nm | 220 | [213] | 220 | [211] |
| Lattice constant | a | nm | 800 | [800] | 900 | [900] |
| Density, soft-core | ρ | μm^{-2} | 1.56 | [1.51] | 1.23 | [1.12] |
| Density, hard-core | ρ | μm^{-2} | 1.56 | [1.55] | 1.23 | [1.22] |

edge-to-edge distance of $d_{\text{min}} = 80$ nm was implemented between all nanocylinders. Each fabricated metasurface covered an area of $2 \times 2 \text{ mm}^2$ and contained more than 6 million nanocylinders.

The center coordinates of the nanocylinders in the array metasurface type are the vertices of a square lattice

$$\mathbf{p}_{ij} = a(\hat{x}i + \hat{y}j) \quad i, j \in \mathbb{Z} \quad (16)$$

where \hat{x} and \hat{y} are Cartesian unit vectors. The center coordinates in the perturbed array \mathbf{P}_{ij} were drawn uniformly from a disk-shaped area centered on each \mathbf{p}_{ij}

$$\mathbf{P}_{ij} = \mathbf{p}_{ij} + R_{ij}(\cos(\Phi_{ij})\hat{x} + \sin(\Phi_{ij})\hat{y}) \quad (17)$$

$$R_{ij} = \frac{a - d - d_{\text{min}}}{2} \sqrt{U_{ij}} \quad (18)$$

$$\Phi_{ij} = 2\pi V_{ij} \quad (19)$$

where $U_{ij}, V_{ij} \in [0, 1]$ are samples from a standard uniform distribution.

The center coordinates in the uniform-type metasurfaces were taken from a generalized Matérn III point process.^[94,95] In this process, points from an initial Poisson point process were deleted with a probability $f(r)$, where r is the distance between any pair of points. The following deletion probability was employed

$$f(r; \alpha, \beta) = \begin{cases} 1 & 0 \leq r < \alpha \\ \frac{\beta - r}{\beta - \alpha} & \alpha \leq r < \beta \\ 0 & \beta \leq r \end{cases} \quad (20)$$

where $\alpha = d + d_{\text{min}}$, $\beta_{\text{soft-core}} = a$ and $\beta_{\text{hard-core}} = \alpha$.

Since all metasurface types of a given resonance case possess very similar average nanocylinder densities and short-range order (compare $r/a < 2$ in Figure 2a), it can be expected that the spectral positions of their electric and magnetic resonances will as well be rather similar. With this consideration in mind, the optical response of the array metasurface type was designed first, and then it was verified that the remaining metasurface types meet the design goals. More precisely, a gradient-based optimization method was used to determine d , h , and a such that in the spectral vicinity of the MD and ED, the transmitted intensity was either maximized and the phase underwent a smooth 2π change (overlapping resonance case), or the intensity was minimized (separate resonance case).

Fabrication: Electron-beam lithography and reactive-ion etching were used to structure a commercially available wafer consisting of a 1 mm-thick amorphous silicon dioxide substrate and a 500 nm-thick amorphous silicon cover layer (Tafelmaier Dünnschicht-Technik GmbH).

First, the thickness of the amorphous silicon layer was reduced to 220 nm via argon-ion-beam etching (Oxford Ionfab 300). Then, the wafer was covered with a 30 nm-thick layer of chromium via ion beam deposition (Oxford Ionfab 300) and a 100 nm-thick layer of electron beam resist (ma_N 2401) via spin-coating. The resist was exposed in a

variable-shaped electron-beam lithography system (Vistec SB 350) and developed in a tetramethylammonium hydroxide solution (AZ MIF 726) for 40 s at room temperature. The resulting resist mask was etched into the chromium layer via argon ion-beam etching and further into the amorphous silicon layer by means of inductively coupled plasma reactive-ion etching (Sentech SI-500 C) with carbon tetrafluoride. The chromium mask and any residual resist were removed with a cerium-based chromium-etching solution and acetone. Finally, the wafer was covered with a 540 nm-thick layer of spin-on glass (Futurrex IC1-200).

Experiments: Four different setups were used for the optical characterization of all fabricated metasurfaces.

All zeroth-order transmittance $T(\lambda)$, reflectance $R(\lambda)$, and diffuse scatterance $Q^D(\lambda)$ spectra were measured in a custom-built incoherent white-light spectroscopy setup with a numerical aperture of 0.044 and full control over the incidence angle and polarization. The reflectance spectra were normalized with respect to a silver mirror. Here, the special case $Q^D = 1 - T - R$ was evaluated.

All phase spectra $\varphi(\lambda)$ were measured in a custom-built Fourier-transform interferometer^[102,103] for normal incidence.

All transmittance $T(\mathbf{r})$ and phase $\varphi(\mathbf{r})$ profiles were measured in a custom-built phase-shifting interferometer for normal incidence and selected wavelengths. A standard four-step Carré method was used for phase retrieval.^[104] The imaging part of this setup had a numerical aperture of about 0.25 and an effective resolution of about 5 μm .

The directional scatterance $Q_{\Omega}(\mathbf{k})$ was obtained from the Fourier plane of a long-working-distance microscope objective (Mitutoyo NIR HR 50X, 0.65 NA), where $d^2I(\mathbf{k})/[dk_x dk_y]$ was measured for each metasurface and the empty setup. The latter provided the incident intensity I_0 . The metasurfaces were placed in the front focal plane of the microscope objective and rotated as to set the incidence angle, reaching a maximum angle of about 20° before touching the microscope objective. Due to this rotation and the limited numerical aperture of the objective, slightly different parts of the \mathbf{k} -space were observed. The dynamic range of the camera (Xenics Xeva-1.7-640-TE3) was artificially extended with a method similar to high-dynamic-range imaging: A sequence of $n = 0..23$ images with exposure times of $2^n \mu\text{s}$ were obtained, which were chosen such that no pixel was overexposed at 1 μs and the noise floor was observed at 2²³ μs . First, all intensity values which did not lie within 15...85% of the dynamic range of the camera were excluded, then the remaining intensity values were scaled by 2^{-n} , and finally the resulting image was constructed by taking the per-pixel-median of the valid and scaled intensity values.

Simulations: For the design of the resonance cases and the retrieval of actual geometric parameters, a finite element method (COMSOL Multiphysics) was used to simulate the transmission coefficient of the array metasurface type. To retrieve the actual geometric parameters, a least-square fit was performed on the experimental transmittance spectra for selected incidence angles $\theta_{in} \in \{0^\circ, 10^\circ, 15^\circ\}$ and both TE and TM polarization.

In all other cases, the local-coordinate T-matrix method was used. The local-coordinate T-matrix method is a reliable tool for the simulation of the electromagnetic response of a large cluster of small particles.^[88,105]

Any electromagnetic field in a homogeneous environment can be expanded in terms of vector spherical harmonics (VSH), which are solutions of the vector Helmholtz equation in spherical coordinates. The incident field and the scattered field of an isolated object can be expanded in terms of^[106]

$$\mathbf{E}_{\text{sca}}(\mathbf{r}) = \sum_{j=1}^{\infty} \sum_{m=-j}^j a_{jm} \mathbf{N}_{jm}^{(3)}(kr) + b_{jm} \mathbf{M}_{jm}^{(3)}(kr) \quad (21)$$

$$\mathbf{E}_{\text{inc}}(\mathbf{r}) = \sum_{j=1}^{\infty} \sum_{m=-j}^j p_{jm} \mathbf{N}_{jm}^{(1)}(kr) + q_{jm} \mathbf{M}_{jm}^{(1)}(kr) \quad (22)$$

where \mathbf{N} and \mathbf{M} are the electric and magnetic vector spherical harmonics, a and b the respective scattering coefficients, and p and q the respective incident coefficients.

The transition matrix (T-Matrix) is a tensor that relates the incident field with the scattered field of one particle in its local-coordinate frame of reference^[106,107]

$$\begin{bmatrix} \mathbf{a} \\ \mathbf{b} \end{bmatrix} = \vec{T} \begin{bmatrix} \mathbf{p} \\ \mathbf{q} \end{bmatrix} \quad (23)$$

The T-matrix describes the electromagnetic response of the particle and is equivalent to the polarizability tensor in Cartesian coordinates.^[108] In this work, the T-matrix (or equivalently the polarizabilities) of the nanocylinders was calculated up to the octupolar order ($j = 3$) by exciting them with the VSH sources^[109] in a commercial Maxwell equation solver (JCMsuite).^[110] Note that for a homogeneous sphere in a homogeneous background medium, the T-matrix can be calculated analytically. For such particles, the T-matrix is a diagonal matrix and the elements are the well-known Mie coefficients with a minus sign according to the formulation used in Equations (21) and (22).^[106,111]

For a cluster of particles with known T-matrices, the incident field at the local coordinate of one particle is given by the global incident field and the scattered field of all other particles. This requires the representation of local coordinates in each other's frame of reference and, hence, the application of the VSH addition theorem.^[112,113] Therefore, to compute the global scattered field of the cluster, a linear set of equations must be solved to obtain the final effective scattering coefficients \mathbf{a}_{eff} and \mathbf{b}_{eff} . This method is called the local-coordinate T-matrix method.^[105]

For a periodic structure, the final scattering coefficients are equal and the equations simplify, but the coherent long-range interaction made the convergence of the coefficients a difficult task that required special care.^[114]

For the simulation of the zeroth-order transmission and reflection coefficients of the disordered metasurfaces, roughly 15² nanocylinders were used and the global scattered field was sampled in a square area that lies parallel and in a distance of 376 nm with respect to the metasurface plane. This distance ensured that the sampling plane does not intersect the circumscribing sphere of any nanocylinder. The sampling area was slightly smaller than the metasurface area to avoid the influence of effects stemming from the edges of the finite-sized metasurfaces. The number of considered nanocylinders were deemed to be sufficient for an accurate description of the metasurfaces' optical response. This is demonstrated by Figure S6a, Supporting Information, which shows the diffuse scatterance of the soft-core uniform metasurface as a function of its size.

For the simulation of the directional scatterance, metasurface sizes of at least $(125 \mu\text{m})^2$ were used to ensure a satisfactory spectral resolution. A cut-and-stitch approach was used since such large metasurfaces are computationally expensive to simulate in one run. In particular, the total metasurface was split into smaller, overlapping patches and each patch was simulated as described in the previous paragraph. The overlaps were chosen such that the sample areas of all patches can directly be stitched together.

Effective Dipole Moments: For an axially symmetric (e.g., spheres, cylinders, etc.), small, and isolated scatterer in a homogeneous nonmagnetic background medium, which is illuminated by plane wave fields \mathbf{E}_{inc} and \mathbf{H}_{inc} along the axis of symmetry, the excited electric \mathbf{p} and magnetic \mathbf{m} dipole moment can be defined as^[115]

$$\mathbf{p} = \varepsilon \alpha^e \mathbf{E}_{\text{inc}} \quad \mathbf{m} = \alpha^m \mathbf{H}_{\text{inc}} \quad (24)$$

where α^e and α^m is the electric and magnetic polarizability, respectively, and $\varepsilon = \varepsilon_0 \varepsilon_{\text{back}}$ is the permittivity of the background.

For a spherical particle, the maximum theoretical polarizability occurs at the resonance wavelength, and the corresponding maximum electric p_0 and magnetic m_0 dipole moment can be written as^[116]

$$p_0 = \frac{6\pi i E_0 \varepsilon}{k^3} \quad m_0 = \frac{6\pi i E_0}{k^3 Z} \quad (25)$$

where E_0 is the amplitude of the incident field, k is the wavenumber, and $Z = \sqrt{\mu/\epsilon}$ the impedance of the background medium. These values were used for normalization.

When there are multiple scatterers, the coupling and rescattering of the particles modifies the scattering coefficients, and the effective dipole moments can be defined based on the effective scattering coefficients^[108,117]

$$\mathbf{p}_{\text{eff}} = \frac{-i\epsilon\sqrt{6\pi}}{k^3} \bar{\bar{\mathbf{F}}}_1 \mathbf{a}_1, \text{eff} \quad (26)$$

$$\mathbf{m}_{\text{eff}} = \frac{-i\sqrt{6\pi}}{Zk^3} \bar{\bar{\mathbf{F}}}_1 \mathbf{b}_1, \text{eff} \quad (27)$$

where

$$\bar{\bar{\mathbf{F}}}_1 = \frac{1}{\sqrt{2}} \begin{bmatrix} 1 & 0 & -1 \\ -i & 0 & -i \\ 0 & \sqrt{2} & 0 \end{bmatrix} \quad (28)$$

Theory of Disordered Huygens' Metasurfaces: For a periodic arrangement of dipolar particles, illuminated by a γ -polarized plane wave, the zeroth-order transmission and reflection coefficient can be calculated as^[117,118]

$$t = 1 + \frac{ik}{2E_0 A} \left(\frac{p_{y,\text{eff}}}{\epsilon} - Zm_{x,\text{eff}} \right) \quad (29)$$

$$r = \frac{ik}{2E_0 A} \left(\frac{p_{y,\text{eff}}}{\epsilon} + Zm_{x,\text{eff}} \right) \quad (30)$$

where $A = a^2$ is the unit cell area, and $p_{y,\text{eff}}$ and $m_{x,\text{eff}}$ are the effective electric and magnetic dipole moments along the y and x -axis, respectively. In an ordered Huygens' metasurface ($p_{y,\text{eff}}/\epsilon + Zm_{x,\text{eff}} = 0$), the electric fields radiated by the electric and magnetic dipoles interfere constructively in transmission and destructively in reflection, resulting in $|t| = 1$ and $r = 0$ for any excitation wavelength. At resonance, it is found that the scattered wave, which is generated by all dipoles, is twice as strong as the incident wave but out of phase ($t = 1 + 2e^{i\pi} = -1$). Section S3, Supporting Information, provides a more detailed description of ordered Huygens' metasurfaces.

If these particles are then brought into an arrangement with isotropic and uniform disorder, the zeroth-order transmission and reflection coefficient may be estimated via

$$t \approx 1 + \frac{ik}{2E_0} \left\langle \frac{p_{x,\text{eff}}}{\epsilon} + Zm_{y,\text{eff}} + \frac{p_{y,\text{eff}}}{\epsilon} - Zm_{x,\text{eff}} \right\rangle_A \quad (31)$$

$$r \approx \frac{ik}{2E_0} \left\langle \frac{p_{x,\text{eff}}}{\epsilon} - Zm_{y,\text{eff}} + \frac{p_{y,\text{eff}}}{\epsilon} + Zm_{x,\text{eff}} \right\rangle_A \quad (32)$$

where $\langle \cdot \rangle_A$ is an area average of the induced moments in all particles. It was shown that lattice variations modulate the effective electric and magnetic moments symmetrically.^[117] Therefore, it can be safely assumed that the equality of the electric and magnetic response is maintained in the presence of isotropic and uniform disorder. In other words, the main components of the electric and magnetic moments in a disordered Huygens' metasurface still satisfy, in average

$$\left\langle \frac{p_{y,\text{eff}}}{\epsilon} + Zm_{x,\text{eff}} \right\rangle_A \approx 0 \quad (33)$$

The cross induced moments $p_{x,\text{eff}}$ and $m_{y,\text{eff}}$ are the result of local random anisotropy. However, due to the uniform positional disorder, these moments vanish in average

$$\langle m_{y,\text{eff}} \rangle_A \approx \langle p_{x,\text{eff}} \rangle_A \approx 0 \quad (34)$$

With this, the transmission and reflection coefficients reduce to a form that is similar to the periodic case

$$t \approx 1 + \frac{ik}{2E_0} \left\langle \frac{p_{y,\text{eff}}}{\epsilon} - Zm_{x,\text{eff}} \right\rangle_A \quad (35)$$

$$r \approx 0 \quad (36)$$

Note that Figure 4e shows the vanishing reflectance and, in particular, $r = 0$ at the resonance wavelength $\lambda = 1.38 \mu\text{m}$. Furthermore, since increasing positional disorder reduces the magnitude of the average effective moments (see Figure 6c), it is possible to obtain $t = 0$ at resonance for a critical degree of positional disorder. More precisely, the magnitude of the average effective dipole moments must reduce to one half of that in the periodic case, such that the incident wave interferes destructively with the zeroth-order component of the scattered wave ($t = 1 + e^{i\pi} = 0$). Last, these relationships can also be observed in Figure S6b and Figure S6c, Supporting Information, which show the mean and standard deviation of the induced moments in the complex plane. Note that the presence of higher-order multipoles led to deviations from the presented theoretical description.

Pair Correlation Function and Structure Factor: The 2D pair correlation function $g(\mathbf{r})$ and the structure factor $S(\mathbf{v})$ of a system of identical particles are related via Fourier transformations^[119]

$$g(\mathbf{r}) = 1 + \frac{1}{\rho} \int_{\mathbb{R}^2} [S(\mathbf{v}) - 1] e^{i2\pi\mathbf{v}\cdot\mathbf{r}} d\mathbf{v} \quad (37)$$

$$S(\mathbf{v}) = 1 + \rho \int_{\mathbb{R}^2} [g(\mathbf{r}) - 1] e^{-i2\pi\mathbf{v}\cdot\mathbf{r}} d\mathbf{r} \quad (38)$$

where ρ is the average particle density.

The scattering intensity S of N particles at positions \mathbf{r}_n

$$S(\mathbf{v}) = \frac{|\eta(\mathbf{v})|^2}{N} \quad \eta(\mathbf{v}) = \sum_{n=1}^N e^{-i2\pi\mathbf{v}\cdot\mathbf{r}_n} \quad (39)$$

is an estimate of the structure factor S in the sense that its ensemble average $\langle S \rangle$ over a large number of realizations tends toward S when all particles are considered^[119]

$$\lim_{N \rightarrow \infty} \langle S(\mathbf{v}) \rangle = \rho \delta(\mathbf{v}) + S(\mathbf{v}) \quad (40)$$

This allows estimation of the pair correlation function g

$$g(\mathbf{r}) \approx \frac{1}{\rho} \int_{\mathbb{R}^2} [\langle S(\mathbf{v}) \rangle - 1] e^{i2\pi\mathbf{v}\cdot\mathbf{r}} d\mathbf{v} \quad (41)$$

The radial pair correlation function $g(r)$ and the radial structure factor $S(v)$ are the azimuthal averages of $g(\mathbf{r})$ and $S(\mathbf{v})$

$$g(r) = \frac{1}{2\pi} \int_{-\pi}^{\pi} g(r \cos(\phi)\hat{\mathbf{x}} + r \sin(\phi)\hat{\mathbf{y}}) d\phi \quad (42)$$

$$S(v) = \frac{1}{2\pi} \int_{-\pi}^{\pi} S(v \cos(\phi)\hat{\mathbf{x}} + v \sin(\phi)\hat{\mathbf{y}}) d\phi \quad (43)$$

where $\hat{\mathbf{x}}$ and $\hat{\mathbf{y}}$ are Cartesian unit vectors.

Probability Density Functions: The standard \bar{f} , folded \check{f} , and wrapped $\circ f$ normal distribution^[120] of a random variable $x \in \mathbb{D}$ were defined as

$$\bar{f}(x; \mu, \sigma) = \frac{1}{\sqrt{2\pi\sigma^2}} \exp\left(-\frac{(x-\mu)^2}{2\sigma^2}\right) \quad \mathbb{D} = [-\infty, \infty] \quad (44)$$

$$\check{f}(x; \mu, \sigma) = \bar{f}(x; \mu, \sigma) + \bar{f}(x; -\mu, \sigma) \quad \mathbb{D} = [0, \infty] \quad (45)$$

$$\circ f(x; \mu, \sigma) = \sum_{n=-\infty}^{\infty} \bar{f}(x; \mu - 2\pi n, \sigma) \quad \mathbb{D} = [-\pi, \pi] \quad (46)$$

The first raw moment (mean) μ_x and the second central moment (variance) σ_x^2 of x are defined as

$$\mu_x = \int_{\mathbb{D}} x f(x) dx \quad \approx \frac{1}{N} \sum_{n=1}^N x_n \quad (47)$$

$$\sigma_x^2 = \int_{\mathbb{D}} (x - \mu_x)^2 f(x) dx \quad \approx \frac{1}{N} \sum_{n=1}^N (x_n - \mu_x)^2 \quad (48)$$

where f is an arbitrary probability density function and the estimates required N samples x_n of x .

The mean and variance of the folded normal distribution are related to the parameters of the underlying standard normal distribution via a transcendental system of equations

$$\mu_x = \sqrt{\frac{2\sigma^2}{\pi}} \exp\left(-\frac{\mu}{2\sigma^2}\right) + \mu \operatorname{erf}\left(\frac{\mu}{\sqrt{2\sigma^2}}\right) \quad (49)$$

$$\sigma_x^2 = \sigma^2 + \mu^2 - \mu_x^2 \quad (50)$$

where $\operatorname{erf}(\cdot)$ is the error function.

For the wrapped normal distribution, the first raw moment (circular moment) of $z = \exp(ix)$ may be considered instead

$$\mu_z = \int_{\mathbb{D}} e^{ix} \circ f(x; \mu, \sigma) dx = e^{-\frac{\sigma^2}{2} + i\mu} \approx \frac{1}{N} \sum_{n=1}^N e^{ix_n} \quad (51)$$

and the mean angle $\hat{\mu}_x$ and circular variance $\hat{\sigma}_x^2$ of x

$$\hat{\mu}_x = \mu = \arg(\mu_z) \quad \hat{\sigma}_x^2 = \sigma^2 = -2\ln(|\mu_z|) \quad (52)$$

are identical to the parameters of the underlying standard normal distribution.

In the kernel density estimation of a 2D probability density function $f(x, y)$, an uncorrelated bivariate standard normal distribution was used as kernel

$$f(x, y) \approx \frac{1}{N} \sum_{n=1}^N \bar{f}(x; x_n, h_x) \bar{f}(y; y_n, h_y) \quad (53)$$

where (x_n, y_n) are N samples of (x, y) , and the constants h_x and h_y are carefully chosen kernel bandwidths. Furthermore, a nonuniform fast Fourier transformation was used in the estimation, and the correct folding or wrapping at the boundaries of the domain of f was accounted for.

Supporting Information

Supporting Information is available from the Wiley Online Library or from the author.

Acknowledgements

D.A. and A.R. contributed equally to this work. This work has been funded by the Deutsche Forschungsgemeinschaft (DFG, German Research Foundation) through the priority program SPP 1839 Tailored Disorder (Project number 278747906, PE 1524/10-2, STA 1426/1-2, CR 3640/7-2). The authors acknowledge support by the Carl Zeiss Foundation and Germany's Excellence Strategy via the Excellence Cluster 3D Matter Made to Order (No. EXC-2082/1-390761711). D.A., S.F., M.F., T.P., and I.S. acknowledge support by the Thuringian State Government within its ProExcellence initiative (ACP²⁰²⁰). A.R. acknowledges support from the Karlsruhe School of Optics and Photonics (KSOP). The authors are also grateful to JCMwave for their free provision of the FEM Maxwell solver JCMsuite.

Open access funding enabled and organized by Projekt DEAL.

Conflict of Interest

The authors declare no conflict of interest.

Data Availability Statement

The data that support the findings of this study are available from the corresponding author upon reasonable request.

Keywords

dielectric metasurfaces, optical diffusers, positional disorder, wavelength-selectivity

Received: July 29, 2021
Revised: October 5, 2021
Published online: December 17, 2021

- [1] A. Egel, U. Lemmer, *J. Quant. Spectrosc. Radiat. Transf.* **2014**, *148*, 165.
- [2] K. Lee, J. Lee, E. Kim, J.-I. Lee, D.-H. Cho, J. T. Lim, C. W. Joo, J. Y. Kim, S. Yoo, B.-K. Ju, J. Moon, *Nanotechnology* **2016**, *27*, 075202.
- [3] Y. Y. Kim, J. J. Park, S. J. Ye, W. J. Hyun, H.-G. Im, B.-S. Bae, O. O. Park, *RSC Adv.* **2016**, *6*, 65450.
- [4] M. A. Golub, A. Averbuch, M. Nathan, V. A. Zheludev, J. Hauser, S. Gurevitch, R. Malinsky, A. Kagan, *Appl. Opt.* **2016**, *55*, 432.
- [5] H. Yilmaz, E. G. van Putten, J. Bertolotti, A. Lagendijk, W. L. Vos, A. P. Mosk, *Optica* **2015**, *2*, 424.
- [6] J. Bertolotti, E. G. van Putten, C. Blum, A. Lagendijk, W. L. Vos, A. P. Mosk, *Nature* **2012**, *491*, 232.
- [7] I. M. Vellekoop, A. Lagendijk, A. P. Mosk, *Nat. Photonics* **2010**, *4*, 320.
- [8] G. Kim, *Eur. Polym. J.* **2005**, *41*, 1729.
- [9] Z. Cai, J. Chen, G. Pedrini, W. Osten, X. Liu, X. Peng, *Light: Sci. Appl.* **2020**, *9*, 143.
- [10] L. Lu, J. Sun, J. Zhang, Y. Fan, Q. Chen, C. Zuo, *Front. Phys.* **2019**, *7*, 77.
- [11] R. A. Hoover, R. G. Hoover, US6963445B2, **2003**.
- [12] N. Antipa, G. Kuo, R. Heckel, B. Mildenhall, E. Bostan, R. Ng, L. Waller, *Optica* **2018**, *5*, 1.
- [13] P. Song, S. Jiang, H. Zhang, Z. Bian, C. Guo, K. Hoshino, G. Zheng, *Opt. Lett.* **2019**, *44*, 3645.
- [14] W. Yang, S. Xiao, Q. Song, Y. Liu, Y. Wu, S. Wang, J. Yu, J. Han, D.-P. Tsai, *Nat. Commun.* **2020**, *11*, 1864.

- [15] T. H. Zhao, G. Jacucci, X. Chen, D.-P. Song, S. Vignolini, R. M. Parker, *Adv. Mater.* **2020**, *32*, 2002681.
- [16] A. K. González-Alcalde, A. Reyes-Coronado, *Opt. Commun.* **2020**, *475*, 126289.
- [17] S. K. Sahoo, D. Tang, C. Dang, *Optica* **2017**, *4*, 1209.
- [18] R. French, S. Gigan, O. L. Muskens, *Opt. Lett.* **2017**, *42*, 1820.
- [19] K. Monakhova, K. Yanny, N. Aggarwal, L. Waller, *Optica* **2020**, *7*, 1298.
- [20] Z. Fang, H. Zhu, Y. Yuan, D. Ha, S. Zhu, C. Preston, Q. Chen, Y. Li, X. Han, S. Lee, G. Chen, T. Li, J. Munday, J. Huang, L. Hu, *Nano Lett.* **2014**, *14*, 765.
- [21] W. Wu, N. G. Tassi, H. Zhu, Z. Fang, L. Hu, *ACS Appl. Mater. Interfaces* **2015**, *7*, 26860.
- [22] T. G. Deepak, G. S. Anjusree, S. Thomas, T. A. Arun, S. V. Nair, A. S. Nair, *RSC Adv.* **2014**, *4*, 17615.
- [23] H. Butt, A. K. Yetisen, A. A. Khan, K. M. Knowles, M. M. Qasim, S. H. Yun, T. D. Wilkinson, *Adv. Opt. Mater.* **2016**, *5*, 1600414.
- [24] R. Schittny, A. Niemeyer, F. Mayer, A. Naber, M. Kadic, M. Wegener, *Laser Photonics Rev.* **2016**, *10*, 382.
- [25] A. P. Mosk, A. Lagendijk, G. Leroose, M. Fink, *Nat. Photonics* **2012**, *6*, 283.
- [26] W. Smith, *Modern Optical Engineering: The Design of Optical Systems*, McGraw-Hill, New York **2007**.
- [27] M. D. Fairchild, *Color Appearance Models*, Wiley, New York **2013**.
- [28] A. Colombo, F. Tassone, F. Santolini, N. Contiello, A. Gambirasio, R. Simonutti, *J. Mater. Chem. C* **2013**, *1*, 2927.
- [29] S. M. Mahpeykar, Y. Zhao, X. Li, Z. Yang, Q. Xu, Z.-H. Lu, E. H. Sargent, X. Wang, *Adv. Opt. Mater.* **2017**, *5*, 1700430.
- [30] M. S. Toivonen, O. D. Onelli, G. Jacucci, V. Lovikka, O. J. Rojas, O. Ikkala, S. Vignolini, *Adv. Mater.* **2018**, *30*, 1704050.
- [31] T. Alqurashi, H. Butt, *ACS Cent. Sci.* **2019**, *5*, 1002.
- [32] F. Lin, L. Zhu, S. Yang, *ACS Appl. Polym. Mater.* **2020**, *2*, 3805.
- [33] T. Ohzono, K. Suzuki, T. Yamaguchi, N. Fukuda, *Adv. Opt. Mater.* **2013**, *1*, 374.
- [34] S. M. Mahpeykar, Q. Xiong, J. Wei, L. Meng, B. K. Russell, P. Hermansen, A. V. Singhal, X. Wang, *Adv. Opt. Mater.* **2016**, *4*, 1106.
- [35] S.-I. Chang, J.-B. Yoon, H. Kim, J.-J. Kim, B.-K. Lee, D. H. Shin, *Opt. Lett.* **2006**, *31*, 3016.
- [36] S. Wadle, D. Wuest, J. Cantalupo, R. S. Lakes, *Opt. Eng.* **1994**, *33*, 213.
- [37] C. Gu, J. Hong, J.-R. Lien, F. Dai, *J. Opt. Soc. Am. A* **1996**, *13*, 1704.
- [38] S. I. Kim, Y. S. Choi, Y. N. Ham, C. Y. Park, J. M. Kim, *Appl. Opt.* **2003**, *42*, 2482.
- [39] R. Pawluczyk, in *Photopolymers and Applications in Holography, Optical Data Storage, Optical Sensors, and Interconnects* (Ed: R. A. Lessard), SPIE, Bellingham, WA, USA **1994**.
- [40] K. S. Lee, B. Jeon, S. W. Cha, *Polym.-Plast. Technol. Eng.* **2011**, *50*, 102.
- [41] H. Butt, K. M. Knowles, Y. Montelongo, G. A. J. Amaratunga, T. D. Wilkinson, *ACS Nano* **2014**, *8*, 2929.
- [42] J. Hu, Y. Zhou, T. Zhang, *Mater. Lett.* **2014**, *136*, 114.
- [43] Y. Ding, X. Li, Z. Zhao, Y. Xiong, S. Guo, *Sci. Rep.* **2019**, *9*, 8665.
- [44] P. Genevet, F. Capasso, F. Aieta, M. Khorasaninejad, R. Devlin, *Optica* **2017**, *4*, 139.
- [45] P. Lalanne, P. Chavel, *Laser Photonics Rev.* **2017**, *11*, 1600295.
- [46] W. T. Chen, F. Capasso, *Appl. Phys. Lett.* **2021**, *118*, 100503.
- [47] N. Yu, F. Capasso, *Nat. Mater.* **2014**, *13*, 139.
- [48] S. Chen, W. Liu, Z. Li, H. Cheng, J. Tian, *Adv. Mater.* **2019**, *32*, 1805912.
- [49] R. Dezert, P. Richetti, A. Baron, *Opt. Express* **2019**, *27*, 26317.
- [50] O. Quevedo-Teruel, H. Chen, A. Díaz-Rubio, G. Gok, A. Grbic, G. Minatti, E. Martini, S. Maci, G. V. Eleftheriades, M. Chen, N. I. Zheludev, N. Papasimakis, S. Choudhury, Z. A. Kudyshev, S. Saha, H. Reddy, A. Boltasseva, V. M. Shalaev, A. V. Kildishev, D. Sievenpiper, C. Caloz, A. Alù, Q. He, L. Zhou, G. Valerio, E. Rajo-Iglesias, Z. Sipus, F. Mesa, R. Rodríguez-Berral, F. Medina, V. Asadchy, S. Tretyakov, C. Craeye, *J. Opt.* **2019**, *21*, 073002.
- [51] H. K. Shamkhi, K. V. Baryshnikova, A. Sayanskiy, P. Kapitanova, P. D. Terekhov, P. Belov, A. Karabchevsky, A. B. Evlyukhin, Y. Kivshar, A. S. Shalin, *Phys. Rev. Lett.* **2019**, *122*, 193905.
- [52] R. Ahmed, M. O. Ozen, M. G. Karaaslan, C. A. Prator, C. Thanh, S. Kumar, L. Torres, N. Iyer, S. Munter, S. Southern, T. J. Henrich, F. Inci, U. Demirci, *Adv. Mater.* **2020**, *32*, 1907160.
- [53] E. Karimi, S. A. Schulz, I. D. Leon, H. Qassim, J. Upham, R. W. Boyd, *Light: Sci. Appl.* **2014**, *3*, e167.
- [54] H.-T. Chen, A. J. Taylor, N. Yu, *Rep. Prog. Phys.* **2016**, *79*, 076401.
- [55] Y. Bao, J. Ni, C.-W. Qiu, *Adv. Mater.* **2019**, *32*, 1905659.
- [56] M. Jang, Y. Horie, A. Shibukawa, J. Brake, Y. Liu, S. M. Kamali, A. Arbabi, H. Ruan, A. Faraon, C. Yang, *Nat. Photonics* **2018**, *12*, 84.
- [57] D. S. Wiersma, *Nat. Photonics* **2013**, *7*, 188.
- [58] S. Yu, C.-W. Qiu, Y. Chong, S. Torquato, N. Park, *Nat. Rev. Mater.* **2021**, *6*, 226.
- [59] S. S. Kruk, C. Helgert, M. Decker, I. Staude, C. Menzel, C. Etrich, C. Rockstuhl, C. Jagadish, T. Pertsch, D. N. Neshev, Y. S. Kivshar, *Phys. Rev. B* **2013**, *88*, 201404.
- [60] M. Castro-Lopez, M. Gaio, S. Sellers, G. Gkantzounis, M. Florescu, R. Sapienza, *APL Photonics* **2017**, *2*, 061302.
- [61] F. Sterl, E. Herkert, S. Both, T. Weiss, H. Giessen, *ACS Nano* **2021**, *15*, 10318.
- [62] G. Osnabrugge, R. Horstmeyer, I. N. Papadopoulos, B. Judkewitz, I. M. Vellekoop, *Optica* **2017**, *4*, 886.
- [63] M. Odeh, M. Dupré, K. Kim, B. Kanté, *Nanophotonics* **2020**, *10*, 705.
- [64] E. Maguid, I. Yulevich, M. Yannai, V. Kleiner, M. L. Brongersma, E. Hasman, *Light: Sci. Appl.* **2017**, *6*, e17027.
- [65] S. Fasold, S. Linß, T. Kawde, M. Falkner, M. Decker, T. Pertsch, I. Staude, *ACS Photonics* **2018**, *5*, 1773.
- [66] S. Jahani, Z. Jacob, *Nat. Nanotechnol.* **2016**, *11*, 23.
- [67] A. I. Kuznetsov, A. E. Miroshnichenko, M. L. Brongersma, Y. S. Kivshar, B. Luk'yanchuk, *Science* **2016**, *354*, aag2472.
- [68] I. Staude, J. Schilling, *Nat. Photonics* **2017**, *11*, 274.
- [69] L. Cong, R. Singh, *Adv. Mater.* **2020**, *32*, 2001418.
- [70] K. Koshelev, Y. Kivshar, *ACS Photonics* **2021**, *8*, 102.
- [71] K. Fan, J. Zhang, X. Liu, G.-F. Zhang, R. D. Averitt, W. J. Padilla, *Adv. Mater.* **2018**, *30*, 1800278.
- [72] J. Proust, F. Bedu, B. Gallas, I. Ozerov, N. Bonod, *ACS Nano* **2016**, *10*, 7761.
- [73] A. P. Ravishankar, M. A. J. van Tilburg, F. Vennberg, D. Visser, S. Anand, *Nanophotonics* **2019**, *8*, 1771.
- [74] I. Staude, A. E. Miroshnichenko, M. Decker, N. T. Fofang, S. Liu, E. Gonzales, J. Dominguez, T. S. Luk, D. N. Neshev, I. Brener, Y. Kivshar, *ACS Nano* **2013**, *7*, 7824.
- [75] M. Decker, I. Staude, M. Falkner, J. Dominguez, D. N. Neshev, I. Brener, T. Pertsch, Y. S. Kivshar, *Adv. Opt. Mater.* **2015**, *3*, 813.
- [76] C. Gigli, Q. Li, P. Chavel, G. Leo, M. L. Brongersma, P. Lalanne, *Laser Photonics Rev.* **2021**, *15*, 2000448.
- [77] A. J. Ollanik, J. A. Smith, M. J. Belue, M. D. Escarra, *ACS Photonics* **2018**, *5*, 1351.
- [78] R. Dezert, P. Richetti, A. Baron, *Phys. Rev. B* **2017**, *96*, 180201.
- [79] K. E. Chong, L. Wang, I. Staude, A. R. James, J. Dominguez, S. Liu, G. S. Subramania, M. Decker, D. N. Neshev, I. Brener, Y. S. Kivshar, *ACS Photonics* **2016**, *3*, 514.
- [80] D. Arslan, K. E. Chong, A. E. Miroshnichenko, D.-Y. Choi, D. N. Neshev, T. Pertsch, Y. S. Kivshar, I. Staude, *J. Phys. D: Appl. Phys.* **2017**, *50*, 434002.
- [81] A. Rahimzadegan, D. Arslan, D. Dams, A. Groner, X. Garcia-Santiago, R. Alaei, I. Fernandez-Corbaton, T. Pertsch, I. Staude, C. Rockstuhl, *Nanophotonics* **2020**, *9*, 75.

- [82] A. Howes, Z. Zhu, D. Curie, J. R. Avila, V. D. Wheeler, R. F. Haglund, J. G. Valentine, *Nano Lett.* **2020**, *20*, 4638.
- [83] Y. Tian, Z. Li, Z. Xu, Y. Wei, F. Wu, *Opt. Mater.* **2020**, *109*, 110358.
- [84] M. Liu, D.-Y. Choi, *Nano Lett.* **2018**, *18*, 8062.
- [85] J. A. Mignaco, *Braz. J. Phys.* **2001**, *31*, 2.
- [86] I. Fernandez-Corbaton *Ph.D. thesis*, Macquarie University, Sydney, Australia **2014**, <https://hdl.handle.net/1959.14/354622>.
- [87] A. Rahimzadegan, M. Fruhnert, R. Alaei, I. Fernandez-Corbaton, C. Rockstuhl, *Phys. Rev. B* **2016**, *94*, 125123.
- [88] A. Rahimzadegan, D. Arslan, R. N. S. Suryadharma, S. Fasold, M. Falkner, T. Pertsch, I. Staude, C. Rockstuhl, *Phys. Rev. Lett.* **2019**, *122*, 015702.
- [89] D. Veksler, E. Maguid, N. Shitrit, D. Ozeri, V. Kleiner, E. Hasman, *ACS Photonics* **2015**, *2*, 661.
- [90] D. Yap, H. Sharifi, D. F. Weston, R. D. Rajavel, US9709711B1, **2013**.
- [91] M.-L. Piao, K.-C. Kwon, H.-J. Kang, K.-Y. Lee, N. Kim, *Appl. Opt.* **2015**, *54*, 5252.
- [92] H. Bertin, Y. Brûlé, G. Magno, T. Lopez, P. Gogol, L. Pradere, B. Gralak, D. Barat, G. Demésy, B. Dagens, *ACS Photonics* **2018**, *5*, 2661.
- [93] H. Yu, K. Lee, J. Park, Y. Park, *Nat. Photonics* **2017**, *11*, 186.
- [94] J. Möller, M. L. Huber, R. L. Wolpert, *Stochastic Process. Appl.* **2010**, *120*, 2142.
- [95] J. Teichmann, F. Ballani, K. G. van den Boogaart, *Spat. Stat.* **2013**, *3*, 33.
- [96] M. A. Klatt, J. Kim, S. Torquato, *Phys. Rev. E* **2020**, *101*, 032118.
- [97] W. C. Chew, *Waves and Fields in Inhomogeneous Media*, IEEE, Piscataway, NJ, USA **1999**.
- [98] R. Paniagua-Domínguez, Y. F. Yu, A. E. Miroshnichenko, L. A. Krivitsky, Y. H. Fu, V. Valuckas, L. Gonzaga, Y. T. Toh, A. Y. S. Kay, B. Luk'yanchuk, A. I. Kuznetsov, *Nat. Commun.* **2016**, *7*, 10362.
- [99] I. N. Bronshtein, K. A. Semendyayev, G. Musiol, H. Mühlig, *Handbook of Mathematics*, Springer, Berlin/Heidelberg, Germany **2015**.
- [100] G. Zhang, S. Torquato, *Phys. Rev. E* **2020**, *101*, 032124.
- [101] P. M. Piechulla, B. Fuhrmann, E. Slivina, C. Rockstuhl, R. B. Wehrspohn, A. N. Sprafke, *Adv. Opt. Mater.* **2021**, *9*, 2100186.
- [102] E. Pshenay-Severin, F. Setzpfandt, C. Helgert, U. Hübner, C. Menzel, A. Chipouline, C. Rockstuhl, A. Tünnermann, F. Lederer, T. Pertsch, *J. Opt. Soc. Am. B* **2010**, *27*, 660.
- [103] E. Pshenay-Severin, M. Falkner, C. Helgert, T. Pertsch, *Appl. Phys. Lett.* **2014**, *104*, 221906.
- [104] P. Carré, *Metrologia* **1966**, *2*, 13.
- [105] R. N. S. Suryadharma, M. Fruhnert, I. Fernandez-Corbaton, C. Rockstuhl, *Phys. Rev. B* **2017**, *96*, 045406.
- [106] M. I. Mishchenko, L. D. Travis, A. A. Lacis, *Scattering, Absorption, and Emission of Light by Small Particles*, Cambridge University Press, Cambridge, UK **2002**.
- [107] P. C. Waterman, *Proc. IEEE* **1965**, *53*, 805.
- [108] J. Mun, S. So, J. Jang, J. Rho, *ACS Photonics* **2020**, *7*, 1153.
- [109] G. Demésy, J.-C. Auger, B. Stout, *J. Opt. Soc. Am. A* **2018**, *35*, 1401.
- [110] X. Garcia-Santiago, M. Hammerschmidt, S. Burger, C. Rockstuhl, I. Fernandez-Corbaton, L. Zschiedrich, *Phys. Rev. B* **2019**, *99*, 045406.
- [111] A. Rahimzadegan, R. Alaei, C. Rockstuhl, R. W. Boyd, *Opt. Express* **2020**, *28*, 16511.
- [112] S. Stein, *Quart. Appl. Math.* **1961**, *19*, 15.
- [113] Y.-I. Xu, *Appl. Opt.* **1995**, *34*, 4573.
- [114] D. Beutel, A. Groner, C. Rockstuhl, I. Fernandez-Corbaton, *J. Opt. Soc. Am. B* **2021**, *38*, 1782.
- [115] J. D. Jackson, *Classical Electrodynamics*, American Association of Physics Teachers, College Park, MD, USA **1999**.
- [116] A. Rahimzadegan, R. Alaei, I. Fernandez-Corbaton, C. Rockstuhl, *Phys. Rev. B* **2017**, *95*, 035106.
- [117] A. Rahimzadegan, T. D. Karamanos, R. Alaei, A. G. Lampranidis, D. Beutel, R. W. Boyd, C. Rockstuhl, arXiv:2108.12364v2 **2021**.
- [118] A. B. Evlyukhin, C. Reinhardt, A. Seidel, B. S. Luk'yanchuk, B. N. Chichkov, *Phys. Rev. B* **2010**, *82*, 045404.
- [119] S. Torquato, *Phys. Rep.* **2018**, *745*, 1.
- [120] J. Patel, *Handbook of the Normal Distribution*, Marcel Dekker, New York **1982**.